

University of Alberta

Analysis of Nanoscale Heat Transport Using
Non-Equilibrium Molecular Dynamics Simulation

by

Choon Ngan Teo

A thesis submitted to the Faculty of Graduate Studies and Research
in partial fulfillment of the requirements for the degree of

Master of Science
in
Chemical Engineering

Department of Chemical and Materials Engineering

©Choon Ngan Teo
Fall 2012
Edmonton, Alberta

Permission is hereby granted to the University of Alberta Libraries to reproduce single copies of this thesis and to lend or sell such copies for private, scholarly or scientific research purposes only. Where the thesis is converted to, or otherwise made available in digital form, the University of Alberta will advise potential users of the thesis of these terms.

The author reserves all other publication and other rights in association with the copyright in the thesis and, except as herein before provided, neither the thesis nor any substantial portion thereof may be printed or otherwise reproduced in any material form whatsoever without the author's prior written permission.

Abstract

A Lennard-Jones gas confined by two parallel solid walls was studied using non-equilibrium Molecular Dynamics, where one-dimensional, steady heat flow was introduced through the gas. Under this condition, the velocity distribution in the direction of heat flow was found to develop skewness and the kurtosis was shown to increase with increasing gas density. In contrast, orthogonal velocity distributions presented no skewness but kurtosis was also found to deviate from equilibrium values. Analysis of statistics conditioned by the sign of molecular velocity showed that the difference in kinetic energy resulted in heat transfer. A proposed adiabatic feedback kurtosis controller, referred to as a kurtostat, manipulates velocity using a differential velocity scaling technique. This controller was used in a test setup to push the gas out of equilibrium without introducing heat flow, and it was found that velocity kurtoses were not independent but weakly coupled with a steady-state gain of approximately 0.16.

Acknowledgements

It is a particular pleasure to thank professors Dr. Phillip Choi and Dr. Larry Kostiuk for their enthusiastic guidance – the numerous discussions on this work with them have been thought-provoking and deeply inspiring for the author.

The author gratefully acknowledges the financial support from the Natural Sciences and Engineering Research Council of Canada, without which this work would not be possible. The author also acknowledges the allocation of computer time by WestGrid, Compute Canada.

Contents

1	Introduction	1
1.1	Background	1
1.2	Literature Review	3
1.3	Present Work	4
2	Methodology	6
2.1	Molecular Dynamics Simulation	6
2.1.1	Force Evaluation	6
2.1.2	Neighbour List	7
2.1.3	Velocity Verlet Integration	9
2.2	Validity of Classical Forces	9
2.3	Interaction Models	10
2.3.1	Gas-phase Intermolecular Interaction	10
2.3.2	Solid-Gas Interaction	11
2.4	Boundary Conditions	11
2.4.1	Periodic Boundaries	11
2.4.2	Solid-Gas Reflective Boundaries	13
2.5	Sampling the Ensemble	14
2.5.1	Kinetic Energy and Temperature	14
2.5.2	Potential Energy	14
2.5.3	Pressure and Heat Flux	14
2.5.4	Skewness and Kurtosis	15
2.6	Simulation Controls	15
2.6.1	Temperature	15

2.6.2	Kurtosis	16
2.7	System Identification	19
2.8	Implementation	19
3	Solid-Gas Systems in Equilibrium	20
3.1	Confined Isolated Gas	21
3.1.1	Simulation Setup	21
3.1.2	System Energy	23
3.1.3	Density Distribution and Adsorption	24
3.1.4	Velocity Distributions	25
3.2	Confined Gas in Thermal Contact with Heat Reservoirs	27
3.2.1	Simulation Setup	27
3.2.2	Temperature, Skewness and Kurtosis	27
4	Heat Diffusion in a Solid-Gas System	30
4.1	Spatial Variation of Statistical Quantities	31
4.1.1	Skewness	31
4.1.2	Kurtosis	31
4.2	Spatial Variation of Conditioned Statistical Quantities	34
4.3	Heat Flux	38
4.3.1	Effect of Pressure	38
4.3.2	Effect of EAC	39
4.4	Thermal Conductivity	41
4.4.1	Fourier's Law	41
4.4.2	Thermal Conductivity of an Ideal Gas	41
4.4.3	Effect of Pressure and Temperature	42
4.4.4	Effect of Pressure and Gap Size	44
4.5	System Pressure	45
4.6	Verification	48
4.6.1	System Size	48
4.6.2	Computer Time	49

5	Velocity Kurtosis of a Gas System – Dynamics and Anisotropy	55
5.1	Motivation	56
5.2	Kurtosis Controller Characterisation	57
5.3	Simulation Setup	59
5.4	Results and Discussion	60
5.4.1	Input Signal and Output Response	60
5.4.2	Steady-State Gain and Error	60
5.4.3	System Noise and Choice of Target Kurtosis	63
5.4.4	Impact on Skewness by Kurtostat	64
6	Conclusions	65
	Bibliography	67

List of Tables

3.1	Lennard-Jones parameters used.	25
4.1	Tabulated results for $T_W = 250$ K and 150 K, $L_z = 6$ nm, $P = 11.3$ atm over various α . *Note: κ computed with small heat fluxes are numerically inaccurate as $Q/\frac{dT}{dz}$ is indeterminate as $Q \rightarrow 0$	50
4.2	Tabulated results for $T_W = 250$ K and 150 K, $L_z = 6$ nm.	51
4.3	Tabulated results for $T_W = 250$ K and 150 K, $L_z = 8$ nm.	52
4.4	Tabulated results for $T_W = 250$ K and 150 K, $L_z = 10$ nm	53
4.5	Tabulated results for $T_W = 200$ K and 100 K, $L_z = 8$ nm.	54

List of Figures

2.1	Illustration of the cut-off distance and the “blind distance”, r_b . Greyed circles represent atoms inside the neighbour list of atom i (middle circle)	8
2.2	Comparison between periodic boundaries (left) versus rigid walls (right). Particles in the grey region are images of the real particle. A particle leaving through the right periodic boundary will re-enter the unit cell from the left, as opposed to a reflection. . .	12
2.3	Probability distribution plots of various reference datasets. In this example, the original data ($n = 1$) is a normal distribution with zero mean ($\mu = 0$) and unity variance ($\sigma^2 = 1$).	18
3.1	The unit cell consists of gaseous argon (light) and immobile copper atoms (dark).	22
3.2	Transient plots of kinetic energy (KE), potential energy (PE) and their sum.	23
3.3	The equilibrium density of argon across the gap, when the solid wall is modelled by Cu (solid line) and M (dotted line). Grey circles represent the positions of copper or M atoms. The arrows indicate the potential cut-off distance from the surface copper or M atom.	24
3.4	Normalised kinetic energy components, skewness and kurtosis across gap.	26
3.5	Illustration of the unit cell (side view). L_x and L_y are lateral dimensions, while L_z is the gap size.	28

3.6	Temperature, velocity skewness and velocity kurtosis (gas in equilibrium).	29
4.1	The probability distribution of velocity sampled from the middle slab reveals a skewed distribution in z .	32
4.2	Temperature, velocity skewness and velocity kurtosis of the gas under steady-state heat flow. It is informative to compare this with the equilibrium case presented in Figure 3.6 (page 29).	33
4.3	Conditioned mass flux, across a hot-to-cold gap. “Left” and “right” refers to the direction of travel of the sampled atoms.	35
4.4	Conditioned momentum flux.	35
4.5	Conditioned heat flux.	36
4.6	Conditioned total potential energy, normalised by area and time.	37
4.7	Heat flux versus system pressure at various gap sizes. Trend lines serve only to guide the eye.	38
4.8	Heat flux versus EAC.	39
4.9	Select temperature gradients versus EAC (labelled), for comparison.	40
4.10	κ versus system pressure at two temperatures (95% confidence intervals shown).	43
4.11	κ versus system pressure at various gap sizes (95% confidence intervals shown).	44
4.12	Deviation from pressure predicted by the ideal gas equation.	46
4.13	Deviation from pressure predicted by the van der Waals equation.	47
4.14	Deviation from pressure predicted by the R-K equation.	47
4.15	Measured κ versus system size (95% confidence intervals shown).	48
4.16	Computer time versus system size.	49

5.1	Evolution of the probability distribution of the dataset.	58
5.2	Kurtosis and skewness of the dataset over iterations.	58
5.3	Block diagram of the system showing the relationship between the ARX models, input and output.	59
5.4	Input signal and output response of the system. Data points are downsampled for clarity.	61
5.5	The solid line (—) and the dotted solid line (—●) are the unit step responses of the ARX models for y_1 and y_2 . Broken lines (---) and (—·) are their 95% confidence intervals, respectively.	62
5.6	Fit on noisy data by the ARX model. The fit for the other output is very similar and is not shown.	63
5.7	Skewness in all three axes over time. The increase in fluctuation is apparent between 2 and 7 ns, which is the period the kurtostat is active.	64

Nomenclature

0	(as subscript) target
α	energy accommodation coefficient
Δt	simulation time step
γ	kurtosis
\hbar	$\frac{h}{2\pi}$, where h is the Planck's constant
κ	thermal conductivity
Λ	de Broglie thermal wavelength
λ	mean free path
\mathbf{a}	acceleration
\mathbf{F}	force
\mathbf{r}	position
\mathbf{v}	velocity
\mathcal{H}	system Hamiltonian
μ	mean
∇	differential operator, or $\hat{x} \frac{\partial}{\partial x} + \hat{y} \frac{\partial}{\partial y} + \hat{z} \frac{\partial}{\partial z}$
\parallel	(as subscript) tangential
\perp	(as subscript) normal or perpendicular
Φ	probability distribution
ϕ	potential
σ	Lennard-Jones parameter, separation where potential is zero

σ	standard deviation
τ	time constant
ε	Lennard-Jones parameter, depth of potential well
A	area
a	ARX model parameter
b	ARX model parameter
C	scaling coefficient for Berendsen thermostat
C_k	modified scaling coefficient for kurtosis controller
$C_{V,m}$	molar heat capacity at constant volume
D_σ	collision diameter
E	energy
e_t	process noise
f	(as subscript) final condition
i	(as index) running index through atoms
i	(as subscript) initial condition
j	(as index) running index through atoms
K	kinetic energy
k	(as index) running index through spatial dimensions
k_B	Boltzmann's constant
K_{ss}	process steady-state gain
L	length
m	mass
N	number of atoms
n	number of moles of substance
N_A	Avogadro's number
n_c	number of collisions
P	pressure

P_c	critical pressure
Q	heat flow
R	universal gas constant
r	distance or separation
S	skewness
T	temperature, thermodynamic
t	time
T_c	critical temperature
T_W	wall temperature for reflective boundary
u_t	process input
V	potential energy
V	volume
v_{ave}	average molecular speed
y_t	process output
z^{-1}	backshift operator

Chapter 1

Introduction

1.1 Background

There are essentially two broad methods of *in-silico* molecular simulation – the stochastic Monte Carlo (MC) method and the deterministic Molecular Dynamics (MD) method. Both aim to collect relevant statistics from the system by exploring its phase-space as quickly and as thoroughly as possible.

In an MC simulation, the system transitions into new states using a Markov chain procedure where a new state is accepted only if it is more energetically favourable than the existing state [1, 2]. Since the system's configuration is the only acceptance criteria during the MC trials, the concept of time and rates such as velocity are irrelevant to this scheme. This entails that only equilibrium properties can be calculated.

MD, on the other hand, computes the trajectories of individual particles precisely. Each particle is treated as a point mass and fundamental equations of motion are numerically integrated to determine its movement at every time step. An excellent introduction to MD is given by Ercolessi [3]. Generally speaking, MD is more suitable for dense systems and when the dynamics is the focus of study, while MC is suitable for dilute systems where only the equilibrium configuration of the system is important.

One typical objective of performing a molecular simulation is to collect time-averaged statistics and estimate the system's thermodynamic states such as temperature, pressure and entropy. Transport coefficients such as thermal conductivity can also be estimated. Molecular simulation is especially useful for simulating nanometer-scale systems and predicting their properties, as many of such systems are too small to perform physical experiments.

The classical-forcefield MD simulator is perhaps the most elaborate product of causal determinism, as envisioned by Laplace in his 1814 *Philosophical Essay on Probabilities* [4]:

“We ought ... to regard the present state of the universe as the effect of its anterior state and as the cause of the one which is to follow. Given for one instant an intelligence which could comprehend all the forces by which nature is animated and the respective situation of the beings who compose it – an intelligence sufficiently vast to submit these data to analysis – it would embrace in the same formula the movements of the greatest bodies of the universe and those of the lightest atom; for it, nothing would be uncertain and the future, as the past, would be present to its eyes.”

Contemporary MD techniques mimic the described “intelligence” to predict future states of the universe based on its current state. Of course, they are neither sufficiently vast nor incorporate formulae arising out of the comprehension of all nature's forces. As a matter of fact, all MD setups justly limit the system size to only the region of interest and many of them apply empirically parameterised potentials (or “force-matching”) to reconcile with experimental observations. Despite this certain level of departure from the first-principles, studies of very specific systems using MD is compensated by its practicality.

1.2 Literature Review

Pioneering research on MD can be traced back to Alder and Wainwright [5], when they studied hard-sphere interactions. Their study offers a general framework of the MD method and shed light on some practical measures to conserve computer resources which was very prohibitive then. Rahman [6] considered a more realistic Lennard-Jones potential and studied the behaviour of liquid argon. Rahman demonstrated, among other things, the accuracy and soundness of MD by comparing the computed self-diffusion constants with experimental data and also showing the diminishing nature of non-Gaussian behaviour over simulation time. In 1967, Verlet [7] made use of what is presently known as the “velocity Verlet integration” and the “Verlet neighbour list” to study the phase diagrams of argon. Verlet’s integration algorithm and the neighbour list device are widely used in MD today.

Owing to the advent of the integrated circuit in the late 1950s and the resulting proliferation of relatively cheap digital computers, there have been tremendous amounts of publication on the success of *equilibrium* MD in predicting the properties of systems over a wide range of complexity and application, including but certainly not limited to the characterisation of biomolecules, nanoparticles, functionalised surfaces, highly non-ideal liquids and crystal defects.

In comparison, non-equilibrium systems are less understood. Unlike equilibrium systems, analytical solutions for non-equilibrium systems, such as from the Boltzmann equation, are intractable except for the simplest cases [8, 9]. Hence, one practical way to study non-equilibrium systems is by extending the application of equilibrium MD and solving them numerically. The very idea of non-equilibrium is too broad and we only focus on 1-dimensional, steady-state heat flow (thermostatic) systems here. Clause and Mareschal [10] explored heat conduction of a dilute hard-sphere gas within confined geometries using MD, and compared the results with a four- and six-moment approximation approach. The walls of the system sandwich the gas and act as heat reservoirs with different temperatures. They analysed the half-ranged statistics of the gas and found good agreement with the six-moment approximation especially at low Knudsen numbers. Shukla and Dhir [11] used a similar non-equilibrium setup involving a sandwiched fluid but with more realistic walls. The tempera-

ture profile of the fluid in the direction of heat flow was found by assuming local thermal equilibrium. Hwang and Kaviani [12] considered the effect of surface properties on the effective thermal conductivity of an argon-filled nanogap, with special consideration to interactions near the triple-point temperature of argon.

For a monatomic fluid in thermal *equilibrium*, the temperature is proportional to the mean-squared velocity of the fluid particles. However, there appear to be regular, convenient mention of temperature in *non-equilibrium* systems. In principle, temperature does not exist if the fluid is not in thermal equilibrium. While slight deviations from equilibrium are generally acceptable for practical calculations, many of such non-equilibrium MD setups found in the literature seem to be lacking in clarity on precisely how far is the deviation.

1.3 Present Work

Exploring a thermally imposed deviation from equilibrium will be one of the objectives of this work. To avoid complications, only similar one-dimensional heat flow systems containing a monatomic, Lennard-Jones gas will be considered. It should first be recognised that an isolated gas in thermal equilibrium should attain Gaussian molecular velocity distributions in any arbitrary direction, and all directions have the same variance. This also means that its molecular speed distribution corresponds to the well-known Maxwell-Boltzmann distribution. However, when the gas conducts heat, its isotropy must necessarily be lost and at least one of the three velocity distributions (e.g. in Cartesian space) should no longer be Gaussian. Thus, the deviation of velocity distribution from Gaussian behaviour will indicate deviation from equilibrium.

In Chapter 2, the general methodology used in this work, including interaction models, boundary conditions, sampling methods and control mechanisms, are presented.

Before embarking on the non-equilibrium cases, equilibrium systems were simulated and the results are presented in Chapter 3. There, we study a micro-

canonical (NVE) ensemble and a canonical (NVT) ensemble to confirm the integrity of the software created for this work. Equilibrium data gathered also serve as reference for non-equilibrium systems.

In Chapter 4, the results and discussion on non-equilibrium, steady-state heat flow systems were presented. The skewness and kurtosis were used to measure precisely how far the velocity distributions deviate from Gaussian behaviour, and how they vary across the direction of heat transfer. In the same chapter, the operating condition was explored to elucidate how temperature, pressure, surface resistance and gap size affect the effective thermal conductivity of the gas. To extract more information from simulation statistics, position and velocity data was split into two sets, conditioned upon the direction of travel of the gas atom at the point of sampling. The nature of heat transfer was studied using such conditioned statistics of mass, momentum, kinetic energy and potential energy.

Work in Chapter 5 was prompted by the findings in Chapter 4. The causal relationship between the kurtosis of velocity in the direction of heat transfer, and the kurtosis of velocity perpendicular to the heat transfer was investigated using a newly developed kurtosis controller.

Lastly, in Chapter 6, the conclusions were summarised and future work recommended.

Chapter 2

Methodology

2.1 Molecular Dynamics Simulation

2.1.1 Force Evaluation

From Newtonian mechanics, the rate of change of velocity of a particle depends on the net force acting on it. Consider a gas particle i in a system comprising of N gas particles. The net force can be evaluated by taking the negative of the spatial gradient of its potential,

$$\mathbf{F}_i = m_i \mathbf{a}_i = -\nabla V(\mathbf{r}_1, \mathbf{r}_2, \dots, \mathbf{r}_N) \quad (2.1)$$

One way to model the system potential is to express it as the sum of pairwise interactions,

$$V(\mathbf{r}_1, \mathbf{r}_2, \dots, \mathbf{r}_N) = \sum_{i=1}^N \sum_{j, j>i}^N \phi(|\mathbf{r}_i - \mathbf{r}_j|) \quad (2.2)$$

It follows that the forces acting on a particle is dependent on the position

of all other particles in the system. It should be noted that the number of pairs to evaluate is $\frac{1}{2}(N^2 - N)$ per time-step, which can be computationally inefficient when N is large [3]. “Neighbour lists” (Section 2.1.2) and potential cut-offs (Section 2.3.1), were implemented in this work and aims to minimise redundant computations and improve computational efficiency. Nevertheless, the evaluation of such non-bonded pairs usually still takes up the largest share of computation time in practice.

It should be noted that many other materials such as metals and semiconductors cannot be modelled accurately with pairwise models and may require more complex, many-body potential models. However, this work mainly deals with the simulation of a noble gas and hence only pairwise potentials will be considered.

2.1.2 Neighbour List

The neighbour list is a computational technique that can eliminate the evaluation of interaction between atom pairs situated too far away from each other.

Firstly, the evaluation of the neighbour list between all pairs is computationally expensive and it is only evaluated every N_u time steps. A “blind distance” is introduced, and defined as

$$r_b = N_u v_{rel,max} \Delta t \quad (2.3)$$

where $v_{rel,max}$ is the maximum relative speed between any two atoms, and Δt is the time step. Hence, r_b the maximum distance an atom can travel before the distance matrix is updated. To avoid missing out atoms which enter the cut-off distance before the neighbour list is updated, an atom’s neighbours are defined as atoms that are less than $r_{cutoff} + r_b$ away (see Figure 2.1). During force evaluations, only forces due to atoms inside the list will be computed. This way, the N^2 scaling of computation time can be minimised as most atoms beyond the cut-off distance (which will return zero interaction forces) are not considered. The scaling of computation time with N can be found in Figure 4.16.

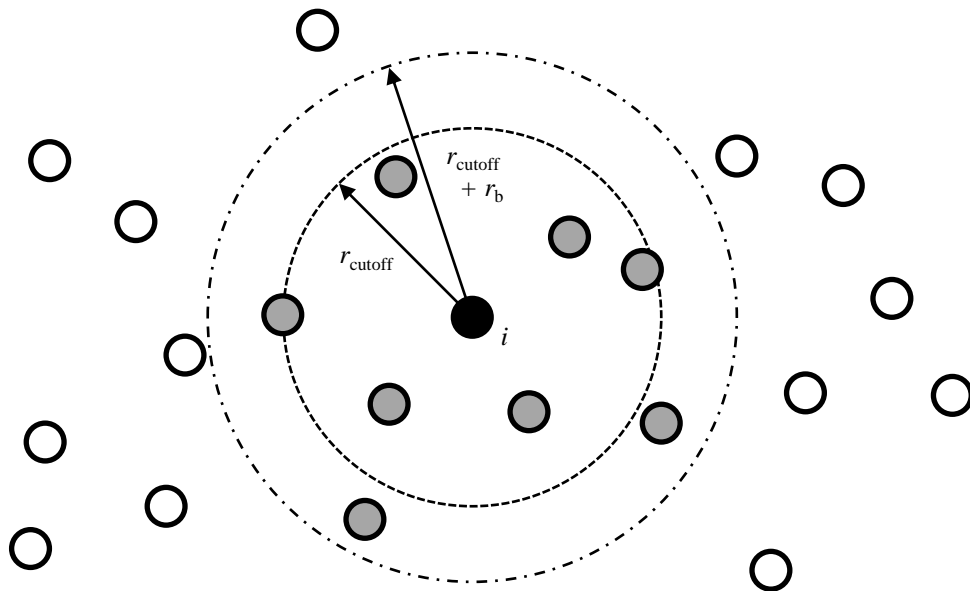


Figure 2.1: Illustration of the cut-off distance and the “blind distance”, r_b . Greyed circles represent atoms inside the neighbour list of atom i (middle circle)

2.1.3 Velocity Verlet Integration

To compute the trajectories of particles in the system, the laws of motion were integrated over time. There exist in literature a wide variety of algorithms to perform this integration, with varying degrees of complexity, numerical accuracy and stability [8]. In this work, the well-known Velocity Verlet algorithm was used. This algorithm is stable, straight-forward to implement, and has excellent energy conservation for Lennard-Jones type potentials.

To advance in time, the following set of equations of motion was evaluated:

$$\mathbf{r}(t + \Delta t) = \mathbf{r}(t) + \mathbf{v}(t) \Delta t + \frac{1}{2} \mathbf{a}(t) \Delta t^2 \quad (2.4)$$

$$\mathbf{v}(t + \Delta t) = \mathbf{v}\left(t + \frac{\Delta t}{2}\right) + \frac{1}{2} \mathbf{a}(t + \Delta t) \Delta t \quad (2.5)$$

where,

$$\mathbf{v}\left(t + \frac{\Delta t}{2}\right) = \mathbf{v}(t) + \frac{1}{2} \mathbf{a}(t) \Delta t \quad (2.6)$$

$$\mathbf{a}(t + \Delta t) = -\frac{1}{m} \nabla V \quad (2.7)$$

As these equations are the result of third-order Taylor expansions, it inevitably suffers from truncation error. The error in position and velocity is in the order of Δt^4 and Δt^2 respectively. Another possible source of error is the machine rounding-off error during floating-point operations, but in practice, it can be assumed negligible owing to the use of 64-bit (“double precision”) floating-point numbers. In all simulations, Δt was chosen to be 10 fs.

2.2 Validity of Classical Forces

In the entirety of this work, only classical forces were considered. Particles were treated as point masses, and quantum effects were neglected. Electronic properties such as chemical bonding and electrical conductivity were therefore not considered as well. To test the validity of classical forces on the system

under investigation, we evaluate its *de Broglie thermal wavelength*, Λ :

$$\Lambda = \sqrt{\frac{2\pi\hbar^2}{mk_B T}} \quad (2.8)$$

where m is the mass of a particle, T is the temperature, k_B is the Boltzmann's constant and \hbar is the reduced Planck's constant. Classical treatment is justified if Λ is small compared to the mean nearest neighbour separation. For a gas, this separation is the mean free path of the gas, which was approximated by

$$\lambda = \frac{V}{\sqrt{2}ND_\sigma} \quad (2.9)$$

where V is the volume, N is the number of gas molecules and D_σ is the collision diameter of the gas. The mean free path is an approximation because the gas was modelled by Lennard-Jones potentials and is not an ideal gas. Accordingly,

$$D_\sigma = \pi \left(\sqrt[6]{2}\sigma_{Ar} \right)^2 \quad (2.10)$$

where σ_{Ar} is the Lennard-Jones parameter of the gas. It can be found that λ/Λ was approximately 44 for the worst case (argon gas at highest pressure, lowest temperature) and 2,300 for the best case, affirming the validity of classical calculations.

2.3 Interaction Models

2.3.1 Gas-phase Intermolecular Interaction

The interactions between gas atoms were governed by a shifted Lennard-Jones (L-J) pair potential,

$$\phi(r_{ij}) = \begin{cases} 4\varepsilon \left[\left(\frac{\sigma}{r_{ij}} \right)^{12} - \left(\frac{\sigma}{r_{ij}} \right)^6 \right] - \phi(r_{cutoff}) & 0 < r < r_{cutoff} \\ 0 & r \geq r_{cutoff} \end{cases} \quad (2.11)$$

where $r_{ij} = |\mathbf{r}_i - \mathbf{r}_j|$. The parameters for argon [13] can be found in Table 3.1. For computational efficiency, the original 12-6 potential function was truncated at $r_{cutoff} = 2.8\sigma_{Ar}$ and shifted upwards by $\phi(r_{cutoff})$. This upwards shift is necessary to avoid a discontinuity of the potential function near r_{cutoff} , which can lead to an unphysical spike of force in that region.

2.3.2 Solid-Gas Interaction

In Chapter 3, the solid wall was modelled as L-J copper atoms in a fixed lattice position. The wall acts as a perfect insulator, and solid-solid interactions were not considered. Again, the parameters for copper [14] can be found in Table 3.1. For the solid-gas pair, the effective L-J parameters can be found by applying the Lorentz-Berthelot mixing rule, given by:

$$\sigma = \frac{1}{2} (\sigma_{Ar} + \sigma_{Cu}) \quad (2.12)$$

and

$$\varepsilon = \sqrt{\varepsilon_{Ar}\varepsilon_{Cu}} \quad (2.13)$$

where the effective σ and ε are the arithmetic mean and geometric mean of their parameters, respectively.

In Chapter 4, the solid wall was modelled as a reflective boundary (see Section 2.4.2), which also acted as a heat transfer surface.

2.4 Boundary Conditions

2.4.1 Periodic Boundaries

Utilising the periodic boundary is a technique for simulating an infinite space with a finite unit cell. When a particle leaves the unit cell through a periodic boundary, it simply re-enters the unit cell from the opposite periodic boundary with the same direction and speed (Figure 2.2).

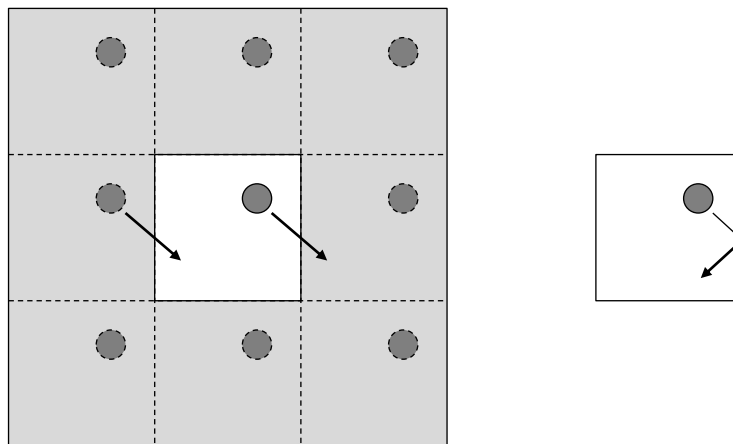


Figure 2.2: Comparison between periodic boundaries (left) versus rigid walls (right). Particles in the grey region are images of the real particle. A particle leaving through the right periodic boundary will re-enter the unit cell from the left, as opposed to a reflection.

The advantage of using periodic boundaries is the removal of undesired wall effects, such as abrupt direction changes if rigid walls are used. By using periodic boundaries, particles can move continuously in a seemingly infinite space.

In order to determine the minimum size of the unit cell, the *minimum image criterion* should be obeyed. This requires that, with the premise that all potentials have a finite cut-off, the longest cut-off diameter of a particle must not be longer than the shortest linear dimension of the unit cell. This criterion is necessary to ensure no particle can ever “see itself” through a periodic boundary, which will almost certainly result in erroneous forces.

One issue with the periodic boundary is that the system may accumulate an overall linear momentum, which in extreme cases, will lead to the so-called “flying ice-cube” effect. This is a computational artefact where the centre of mass of the system moves through periodic boundaries but its constituent particles are not moving relative to each other. Initial conditions and certain control mechanisms such as Berendsen-type thermostats may artificially create this net momentum drift. To prevent this, the overall linear momentum is removed in the direction of periodicity at every 5% progress in simulation.

2.4.2 Solid-Gas Reflective Boundaries

To implement the wall of a heat reservoir, the concept of energy accommodation [15] needs to be mentioned. The energy accommodation coefficient (EAC) takes a value between 0 and 1 and it describes the thermalisation efficiency between a gas and a surface. EAC is defined by

$$\alpha = \frac{\langle E_f - E_i \rangle}{\langle E_s - E_i \rangle} \quad (2.14)$$

where E_f and E_i is the scattered (final) and initial gas molecular energy respectively, and E_s is the average energy of the gas when it has the same temperature of the wall, T_W . Clearly, the wall acts as a perfect thermal insulator if $\alpha = 0$ and a perfect heat transfer surface if $\alpha = 1$.

The wall was modelled by reflecting any gas atoms and mimicking the effect of energy accommodation. At every instance of impingement by a gas atom, the simulation decides randomly whether the atom must be *diffusively* or *specularly* reflected back into the bulk, where the respective probabilities are α and $1 - \alpha$. For a specular reflection, the velocity component normal to the wall was simply inverted, with no change in overall speed or in tangential velocity components. For a diffuse reflection, the velocity components tangential to the wall were assigned by drawing randomly from a normal distribution with a variance of $k_B T_W / m$, i.e.:

$$\Phi(v_{\parallel}) = \frac{1}{\sqrt{2\pi k_B T_W / m}} \exp\left(\frac{-v_{i,\parallel}^2}{2k_B T_W / m}\right) \quad (2.15)$$

while the velocity component normal to the wall was drawn from

$$\Phi(v_{\perp}) = \frac{|v_{i,\perp}|}{const.} \exp\left(\frac{-v_{i,\perp}^2}{2k_B T_W / m}\right) \quad (2.16)$$

The total probability of the probability density function (PDF) in Eq. (2.16) was normalised naturally to unity as a rejection-sampling method was used.

2.5 Sampling the Ensemble

2.5.1 Kinetic Energy and Temperature

The equilibrium gas temperature was estimated using the well-known equipartition formula:

$$K = \frac{1}{2} \sum_{i=1}^N m_i \mathbf{v}_i^2 = \frac{3}{2} N k_B T \quad (2.17)$$

2.5.2 Potential Energy

The potential energy of a particle i is given by

$$V_i = \frac{1}{2} \sum_{j \neq i}^N \phi(r_{ij}) \quad (2.18)$$

where ϕ is determined from Eq. (2.11). The system (total) potential energy can be found by evaluating Eq. (2.2).

2.5.3 Pressure and Heat Flux

The pressure on the reservoir walls was determined by computing the averaged, time rate of change of the normal momentum of gas atoms that impinges the wall, i.e.,

$$P = \sum_{i=1}^{n_c} (m_i v_{\perp,i,out} - m_i v_{\perp,i,in}) / (At) \quad (2.19)$$

where A is the wall area, t is the total time, and n_c is the number of impingements during that time.

Similarly, the heat fluxes through the reservoir walls were computed by considering the difference between the normal incoming kinetic energy, $K_{\perp,i,in}$, and the normal outgoing kinetic energy, $K_{\perp,i,out}$, of all impinging gas atoms, over

time and area:

$$\frac{q}{At} = \sum_{i=1}^{n_c} (K_{\perp,i,out} - K_{\perp,i,in}) \quad (2.20)$$

2.5.4 Skewness and Kurtosis

It is of particular interest in this work to find the amount of deviation of the velocity PDF from the normal distribution. To quantify this deviation, skewness (S) and kurtosis (γ), which respectively is the third and fourth standardised central moment, was considered. Skewness indicates the asymmetry of PDF's shape, while kurtosis indicates the ‘‘peaked-ness’’ and/or presence of heavy-tails of the PDF. The skewness of a velocity distribution is given by

$$S = \frac{\mu_3}{\sigma^3} = \frac{\langle (v_i - \hat{\mu})^3 \rangle}{\langle (v_i - \hat{\mu})^2 \rangle^{3/2}} \quad (2.21)$$

while its kurtosis is given by

$$\gamma = \frac{\mu_4}{\sigma^4} = \frac{\langle (v_i - \hat{\mu})^4 \rangle}{\langle (v_i - \hat{\mu})^2 \rangle^2} \quad (2.22)$$

A normal distribution has a skewness of exactly zero and has a kurtosis of exactly three. It should be noted that in the literature, kurtosis may also be reported as ‘‘excess kurtosis’’, which is the kurtosis minus three.

2.6 Simulation Controls

2.6.1 Temperature

Where it was desired to equilibrate the system to a particular temperature, the Berendsen thermostat [16] was used. This thermostat is a feedback temperature control mechanism that scales the velocities of all i atoms by a factor

of C :

$$v_{i,scaled} = Cv_i \quad (2.23)$$

where

$$C = \sqrt{1 + \frac{\Delta t}{\tau} \left(\frac{T_0}{T} - 1 \right)} \quad (2.24)$$

T_0 is the target temperature, T is the instantaneous system temperature, Δt is the simulation time step and τ is the time constant.

The instantaneous system temperature was estimated by Eq. (2.17). The time constant should be small enough so that the system can be quickly equilibrated to the new temperature but not too small to cause undesired high frequency fluctuations in temperature. In all simulations, the time constant was chosen to be $100 \times \Delta t$.

2.6.2 Kurtosis

In Chapter 5, it is of interest to find the causal relationship between kurtosis of the velocity distribution in the direction of heat flow ($\gamma_{v\parallel}$) and kurtosis of the velocity distribution normal to the direction of heat flow ($\gamma_{v\perp}$). To do that, a technique was needed to manipulate $\gamma_{v\parallel}$ in the simulation so that its effect on $\gamma_{v\perp}$ can be observed. Little can be found in literature on how to manipulate the kurtosis in MD simulations and hence the following feedback, constant-energy kurtosis controller was proposed.

The reader should be cautioned upfront that controlling kurtosis is an unconventional approach. This is because kurtosis is generally a resulting statistic of a distribution and not a cause. Manipulating kurtosis is also unphysical unless it is suspected that an underlying physical process can alter it. It should also be noted that the relationship between kurtosis and the shape of the distribution is a one-to-many relationship. For example, a normal distribution has a kurtosis of three, but a distribution with a kurtosis of three may not necessarily mean it is a normal distribution. Nevertheless, one advantage of using the proposed controller was the removal of temperature and density gradients,

which was necessary to drive the system out of equilibrium and generate kurtosis at the first place. Their removal from the system allowed the study of the relationship between $\gamma_{v\parallel}$ and $\gamma_{v\perp}$ in isolation.

To implement the kurtosis controller, a modified scaling coefficient, C_k , was first defined:

$$C_k = -1 + \sqrt{1 + \frac{\Delta t}{\tau} \left(\frac{\gamma_0}{\gamma} - 1 \right)} \quad (2.25)$$

where γ_0 is target kurtosis and γ is the ‘‘instantaneous kurtosis’’. This scaling coefficient is a simple downward shift of the scaling factor used in the Berendsen thermostat. Next, an intermediate, reference dataset, v_{ref} , was computed:

$$v_{i,ref} = v_i \times |v_i|^{n-1}, \quad n \geq 1 \quad (2.26)$$

where n is a constant that dictates the excess kurtosis of the reference velocity dataset. For example, if $n = 2$, then the reference dataset is the square of the original function. The reference dataset always has a kurtosis greater or equal to the original data. The absolute operator handles even-numbered exponents to ensure the symmetry of the reference dataset (e.g., $v_i^4 \neq v_i |v_i|^3$). A small n results in slower response, while a large n may lead to numerical instability. $n = 2$ was used throughout this work, although values between 1.5 and 3 are reasonable. Figure 2.3 shows how various reference datasets compare with a Gaussian dataset.

Next, the original velocities are redistributed by differential scaling of the velocities:

$$v_{i,rd} = v_i + C_k (v_{i,ref} - v_i) \quad (2.27)$$

where $v_{i,ref} - v_i$ is the error between the (desired) reference velocity and the current velocity, and C_k acts as a gain term for the adjustment. Finally, v_{rd} was normalised to maintain overall kinetic energy:

$$v_{i,new} = \left(\frac{\sum m_i v_i^2}{\sum m_i v_{i,rd}^2} \right) v_{i,rd} \quad (2.28)$$

Further tests and an application of this kurtosis controller can be found in Chapter 5.

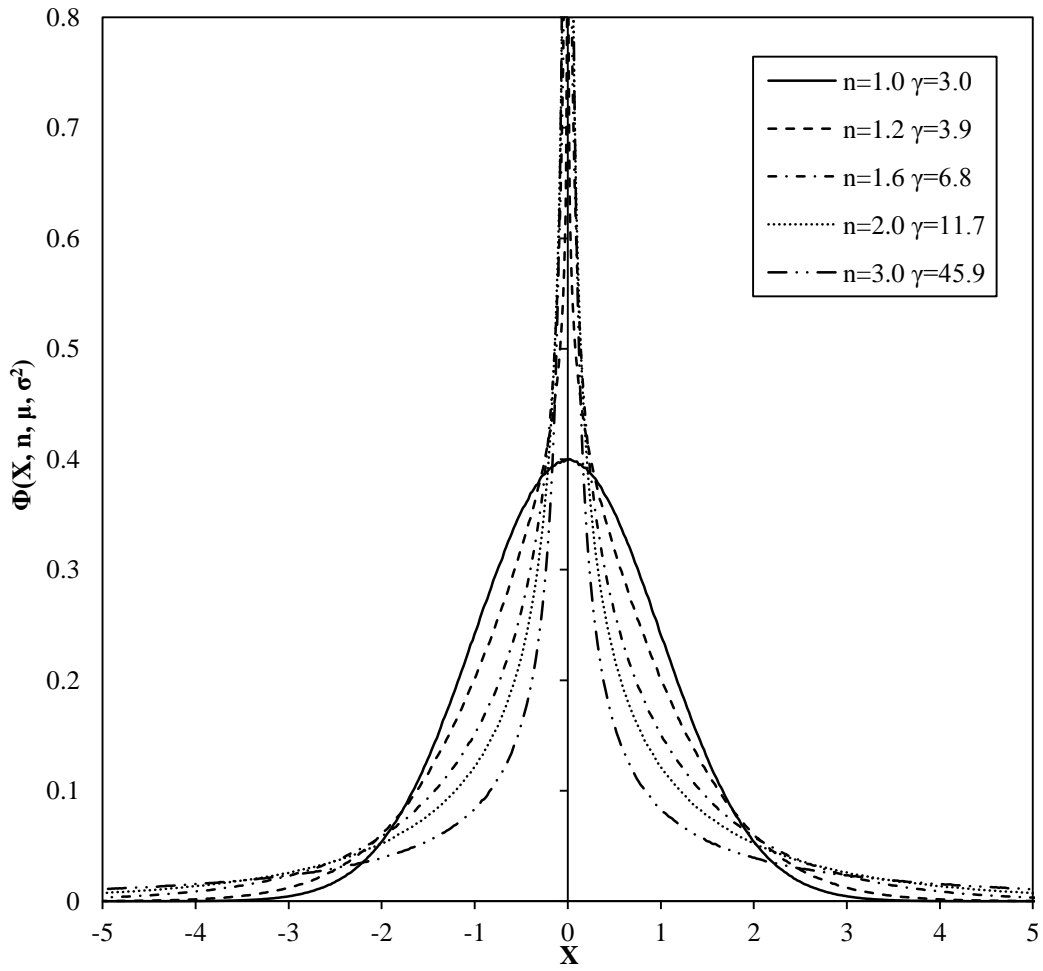


Figure 2.3: Probability distribution plots of various reference datasets. In this example, the original data ($n = 1$) is a normal distribution with zero mean ($\mu = 0$) and unity variance ($\sigma^2 = 1$).

2.7 System Identification

In Chapter 5, the dynamic response of kurtosis was studied using statistical analysis. The ARX model (AutoRegressive model with eXogenous inputs) is a simple linear model used for fitting discrete time, input-output data from dynamic systems. For input \mathbf{u} to a dynamic system corrupted by noise \mathbf{e} , the output \mathbf{y} is modelled by [17]:

$$(1 + a_1z^{-1} + a_2z^{-2} + \dots + a_{na}z^{-na}) y_t = (b_1z^{-1} + b_2z^{-2} + \dots + b_{nb}z^{-nb}) u_t + e_t \quad (2.29)$$

where $a_{1\dots na}$ and $b_{1\dots nb}$ are the model parameters, na and nb are the orders of the \mathbf{a} and \mathbf{b} polynomials, and z^{-1} is the backshift operator. The parameters were estimated by using the SYSTEM IDENTIFICATION TOOLBOX in MATLAB. The steady-state (*ss*) gain, K_{ss} , can be easily evaluated by setting all $\mathbf{u} = u_{ss} = 1$ and making y_{ss} the subject, i.e.,

$$K_{ss} = \frac{y_{ss}}{u_{ss}} = \frac{b_1 + b_2 + \dots + b_{nb}}{1 + a_1 + a_2 + \dots + a_{na}} \quad (2.30)$$

2.8 Implementation

The computer code used in this work was written in MATLAB R2010b with the DISTRIBUTED COMPUTING TOOLBOX and SYSTEM IDENTIFICATION TOOLBOX. Code execution was performed remotely at the Western Canada Research Grid (“WestGrid”) Orcinus facility. The code was single-threaded but multiple MD system configurations were typically executed in parallel. Orcinus nodes utilise the Intel Xeon X5650 six-core processor running at 2.66 GHz, and each node is equipped with 24 GB of memory.

Chapter 3

Solid-Gas Systems in Equilibrium

In this chapter, two equilibrium systems were set up. Both involve argon gas several nanometres thick sandwiched by two solid walls. In the first part of this chapter, a microcanonical (NVE) ensemble was simulated. The walls were explicitly modelled as copper atoms that interact with the gas via Lennard-Jones potentials. However, the copper atoms are immobile and thermal insulating. A canonical (NVT) ensemble was simulated in the second part of this chapter. The copper walls were replaced by reflective walls that act as heat reservoirs. Overall, work in this chapter serves to affirm the integrity of the software created for this work and to generate reference equilibrium data for the upcoming non-equilibrium simulations in Chapter 4.

3.1 Confined Isolated Gas

In this section, an NVE ensemble containing argon gas sandwiched between two copper walls was simulated. The main objective of this section is to verify the independence of kinetic energy and potential energy terms in the system Hamiltonian, presumed as:

$$\mathcal{H}(\mathbf{r}, \mathbf{v}) = V(\mathbf{r}) + K(\mathbf{v}) \quad (3.1)$$

or more explicitly,

$$\mathcal{H}(\mathbf{r}, \mathbf{v}) = \sum_{i=1}^N \sum_{j, j>i}^N \phi(|\mathbf{r}_i - \mathbf{r}_j|) + \frac{1}{2} \sum_{i=1}^N m_i \mathbf{v}_i^2 \quad (3.2)$$

One indicator of separation between V and K is that the velocity distribution of the gas is independent of its position. In this chapter, walls were introduced to exert a potential field external to the gas. The walls are thermally insulating, but have considerable influence on the gas via L-J potentials. Despite the presence of walls (or wall geometry), it is to be expected that the gas velocities should still be Gaussian in all directions and obeys energy equipartition at any point in the gas.

3.1.1 Simulation Setup

The solid wall was modelled by three layers of copper atoms, placed in a $10 \times 10 \times 3$ basic cubic lattice with each particle separated by a distance of $\sqrt[6]{2}\sigma_{Cu}$ (see Table 3.1 for value of σ_{Cu}). The copper atoms were immobile but were allowed to influence the argon atoms. As shown in Figure 3.1, two such walls were placed at the top and bottom of the unit cell (z direction), while periodic boundaries were placed laterally (x and y directions). Due to cut-off potentials and the periodic boundaries, argon atoms can neither “see through” the thickness nor edges of the wall, and so the wall will appear to extend infinitely beyond the edges of the unit cell.

The total simulation horizon was 1 ns. For the first 10% of simulation (or 100 ps), the system temperature was brought to about 220 K by the thermostat and then switched off. Data was recorded only after 200 ps to allow time for equilibration. The number of argon and copper atoms used was 245 and 600, respectively.

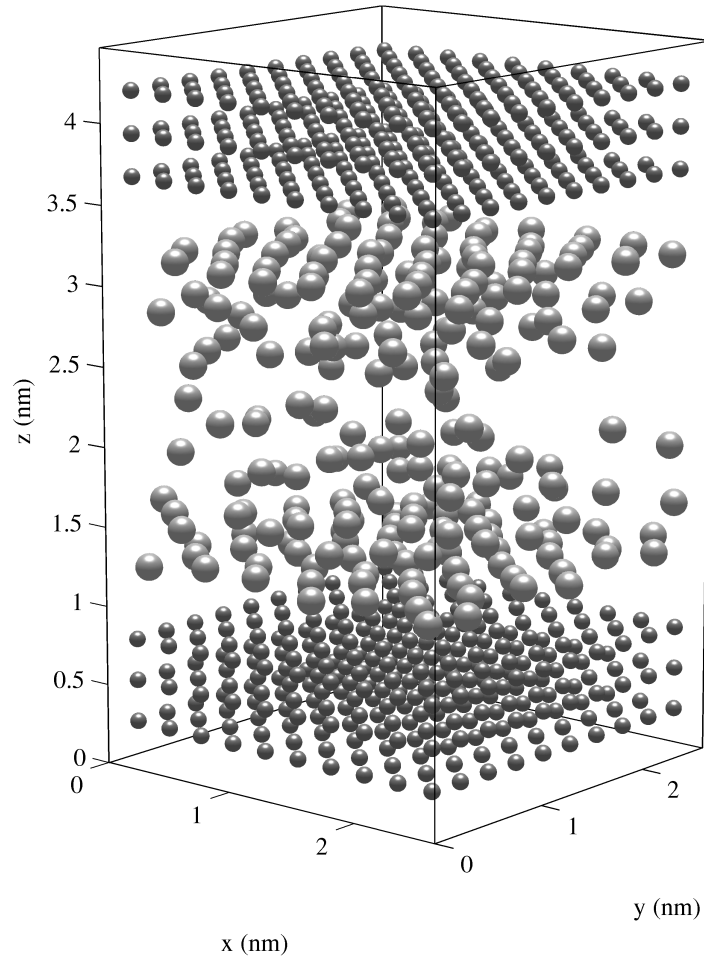


Figure 3.1: The unit cell consists of gaseous argon (light) and immobile copper atoms (dark).

3.1.2 System Energy

For an NVE ensemble, energy conservation of the system is paramount and it was verified by plotting the system energy over time. From Figure 3.2, the system energy remained constant and did not fluctuate once the thermostat was turned off.

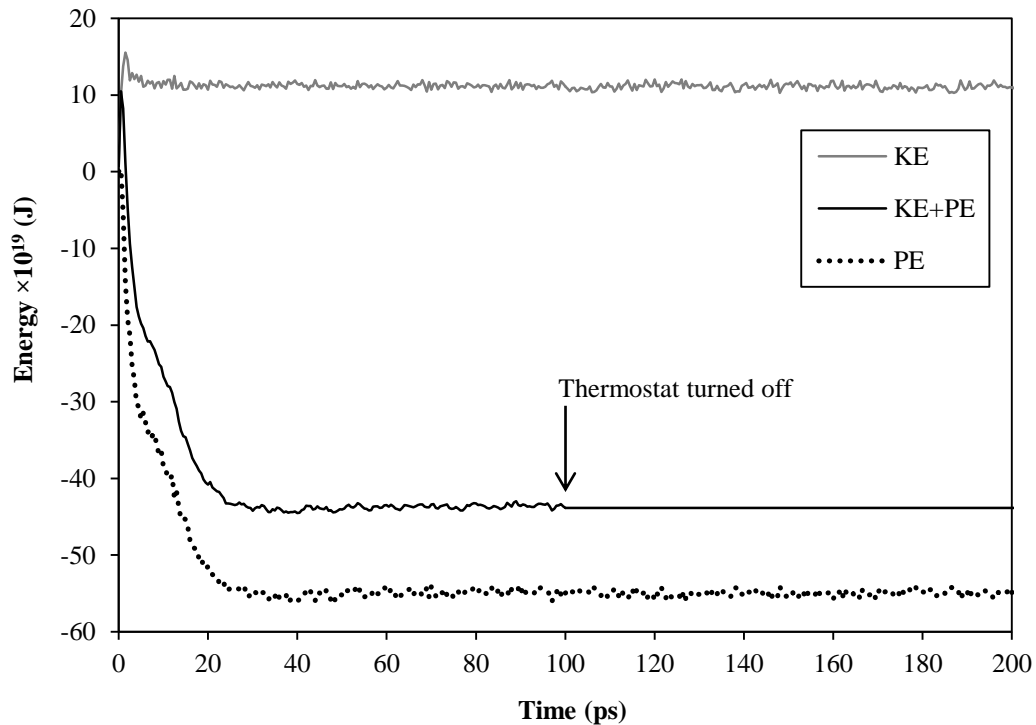


Figure 3.2: Transient plots of kinetic energy (KE), potential energy (PE) and their sum.

3.1.3 Density Distribution and Adsorption

Here, the equilibrium density distribution of argon was studied. From Figure 3.3, argon atoms form a very distinct layer over copper atoms due to adsorption. Second and third layers are also visible in diminishing densities and they are largely due to attractive forces from the adsorbed layer. This layered structure was expected and also observed in a similar work [11].

For comparison, and only in this section, walls made of a hypothetical substance, “M”, was used in place of copper. M has a much weaker attractive potential but a larger radius compared to copper (Table 3.1 shows the L-J parameters of M). As expected, less argon was adsorbed, and the adsorbed layer was found further away from the wall.

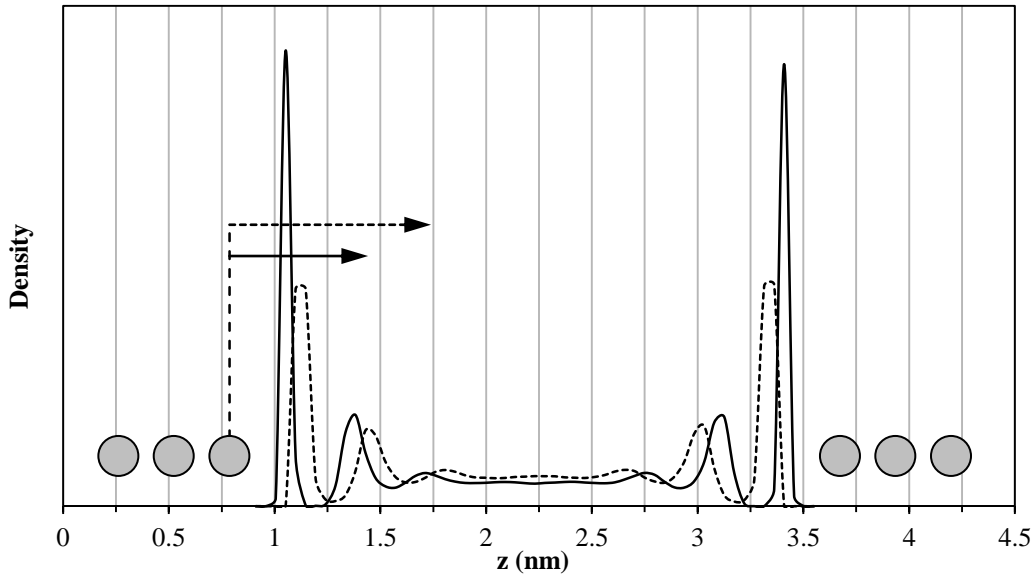


Figure 3.3: The equilibrium density of argon across the gap, when the solid wall is modelled by Cu (solid line) and M (dotted line). Grey circles represent the positions of copper or M atoms. The arrows indicate the potential cut-off distance from the surface copper or M atom.

Table 3.1: Lennard-Jones parameters used.

Substance	$\sigma \times 10^{-10}$ (m)	ϵ / k_B (K)
Ar	3.4	120
Cu	2.338	4750
M	3.4	713

3.1.4 Velocity Distributions

The volume of gas was divided into 11 equal parts (or “slabs”) along the z -axis for sampling.

From Figure 3.4, it can be seen that the normalised variances of velocity were approximately equal to each other, with no appreciable trend with respect to its z -location. In particular, the variances in the z -axis remained unaffected even for gas atoms very near the surface. This observation confirms the equipartition of energy which predicts that, the energy for a monatomic gas is equal in all its degrees of freedom (x -, y - and z - axes) when in equilibrium.

Having established the equipartition of energy, the next step was to verify whether the sets of velocity are Gaussian. One way to do so is to plot the data points on a normal probability plot, and then verify if the points fall on a straight line. Another way, which was done here, is to compute the skewness (Eq. (2.21)) and kurtosis (Eq. (2.22)) of the data and check if they deviate from that of a normal distribution's. From Figure 3.4, it can be seen that the skewness and kurtosis of velocity hardly deviate from zero and three, respectively. This indicates that the velocity distributions in all directions follow the normal distribution, with no apparent influence from the wall. Hence, it can be concluded that at equilibrium, the velocity of gas atoms are independent of position and their speeds follow the Maxwell-Boltzmann distribution.

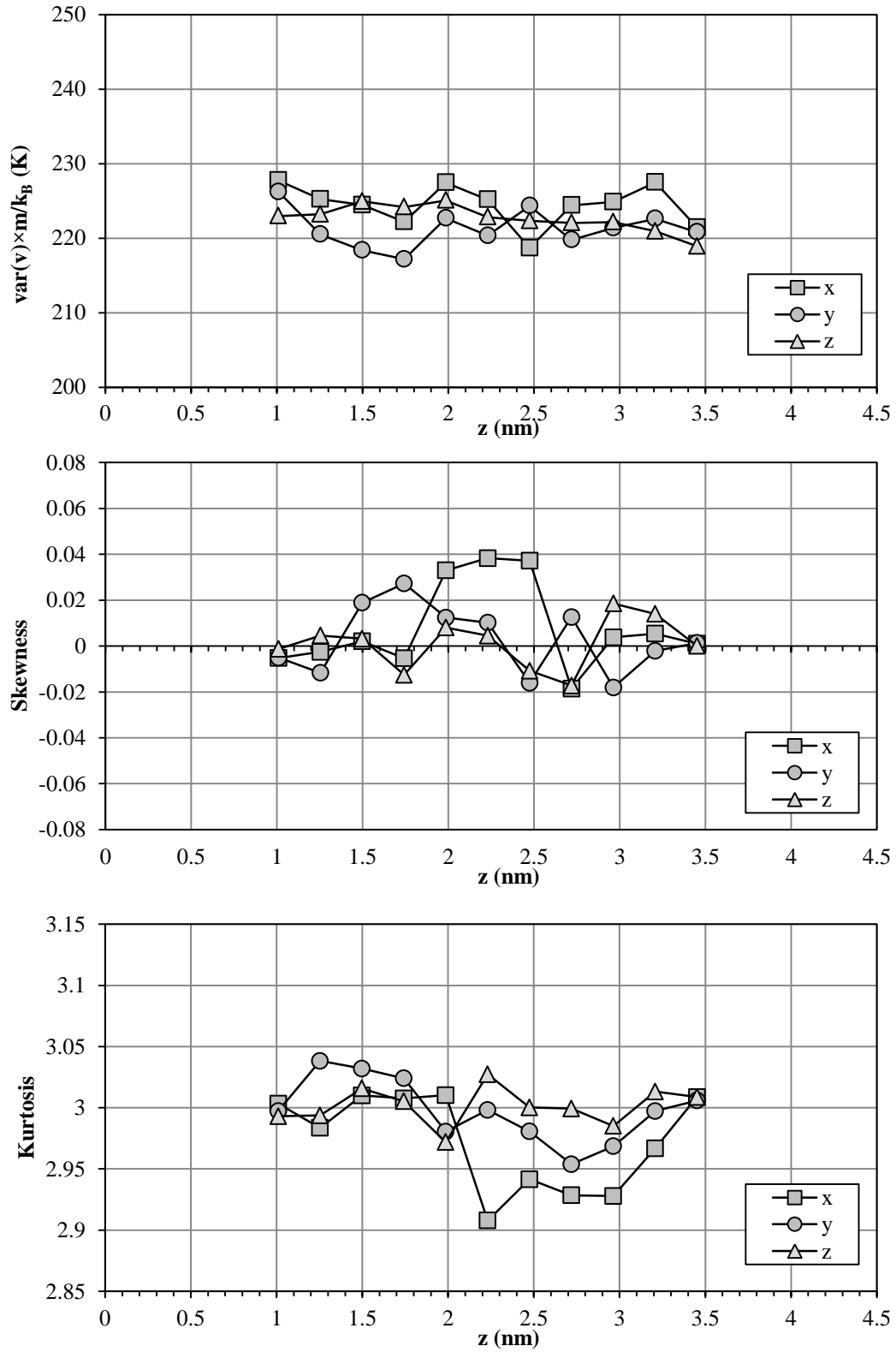


Figure 3.4: Normalised kinetic energy components, skewness and kurtosis across gap.

3.2 Confined Gas in Thermal Contact with Heat Reservoirs

3.2.1 Simulation Setup

In this section, an NVT ensemble containing argon gas sandwiched between two reflective walls (see Section 2.4.2 for description) was simulated. Figure 3.5 shows the arrangement and orientation of the unit cell.

To create a base case where there is no temperature gradient and no heat flow, both walls were set at 200 K and were placed 8 nm apart (1 nm and 9 nm mark of the unit cell). The unit cell is 14×14 nm in lateral directions. 512 argon atoms were placed in the unit cell, which translates to an ideal gas pressure of about 9 atm. Unless specified, the energy accommodation coefficients (α) of the walls were set at exactly 1, which implies that the walls are perfect heat transfer surfaces, but it should be noted that temperature slip (or interfacial temperature jump) will still occur if there is heat flow [15]. The walls do not generate potentials and hence gas atoms do not adsorb to the surface.

The simulation horizon was chosen to be 7 ns, with $\Delta t = 10$ fs. The thermostat was used initially to adjust the system temperature, and was switched off after 100 ps. Thermostat action only serves to bring the system to the expected, average temperature quickly. Data was recorded after 1 ns to allow time for equilibration. Again, the volume of gas was divided into 11 equal slabs along the L_z for analysis.

3.2.2 Temperature, Skewness and Kurtosis

The temperature, skewness and kurtosis trends along the z -axis are presented in Figure 3.6. The skewness and kurtosis fluctuates about zero and three respectively, with no clear trend. Similar to the NVE ensemble, we conclude that at equilibrium, the velocity of gas atoms are independent of position and follow the Maxwell-Boltzmann distribution.

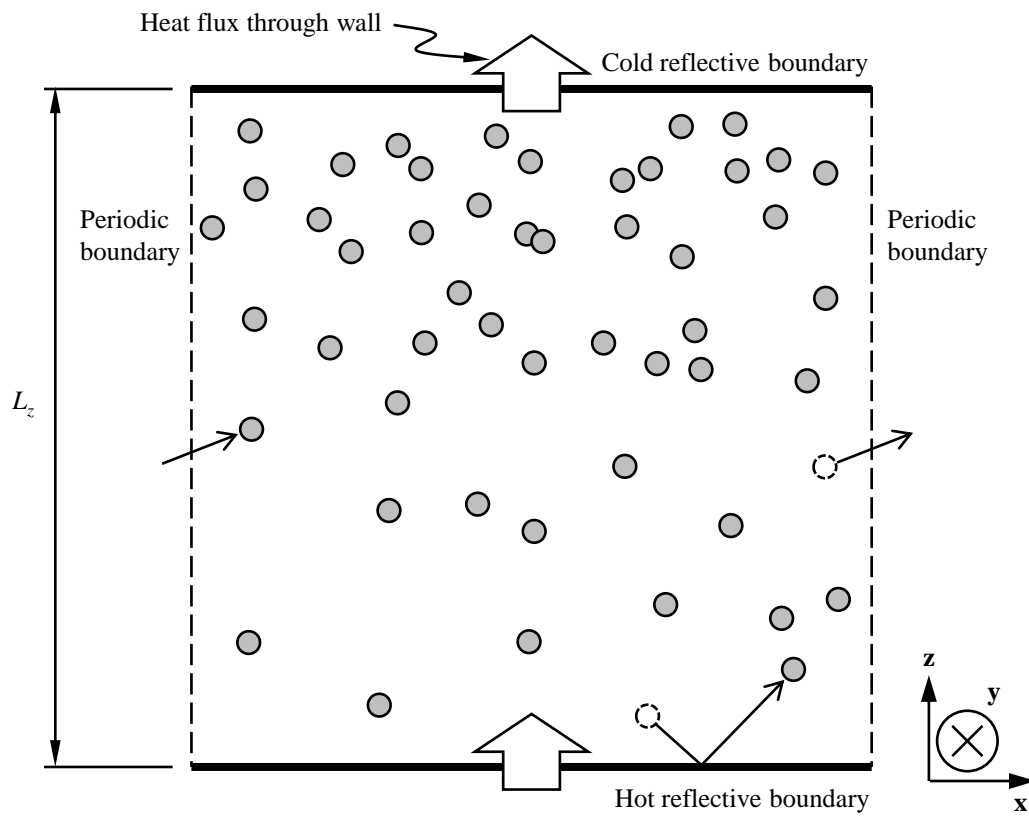


Figure 3.5: Illustration of the unit cell (side view). L_x and L_y are lateral dimensions, while L_z is the gap size.

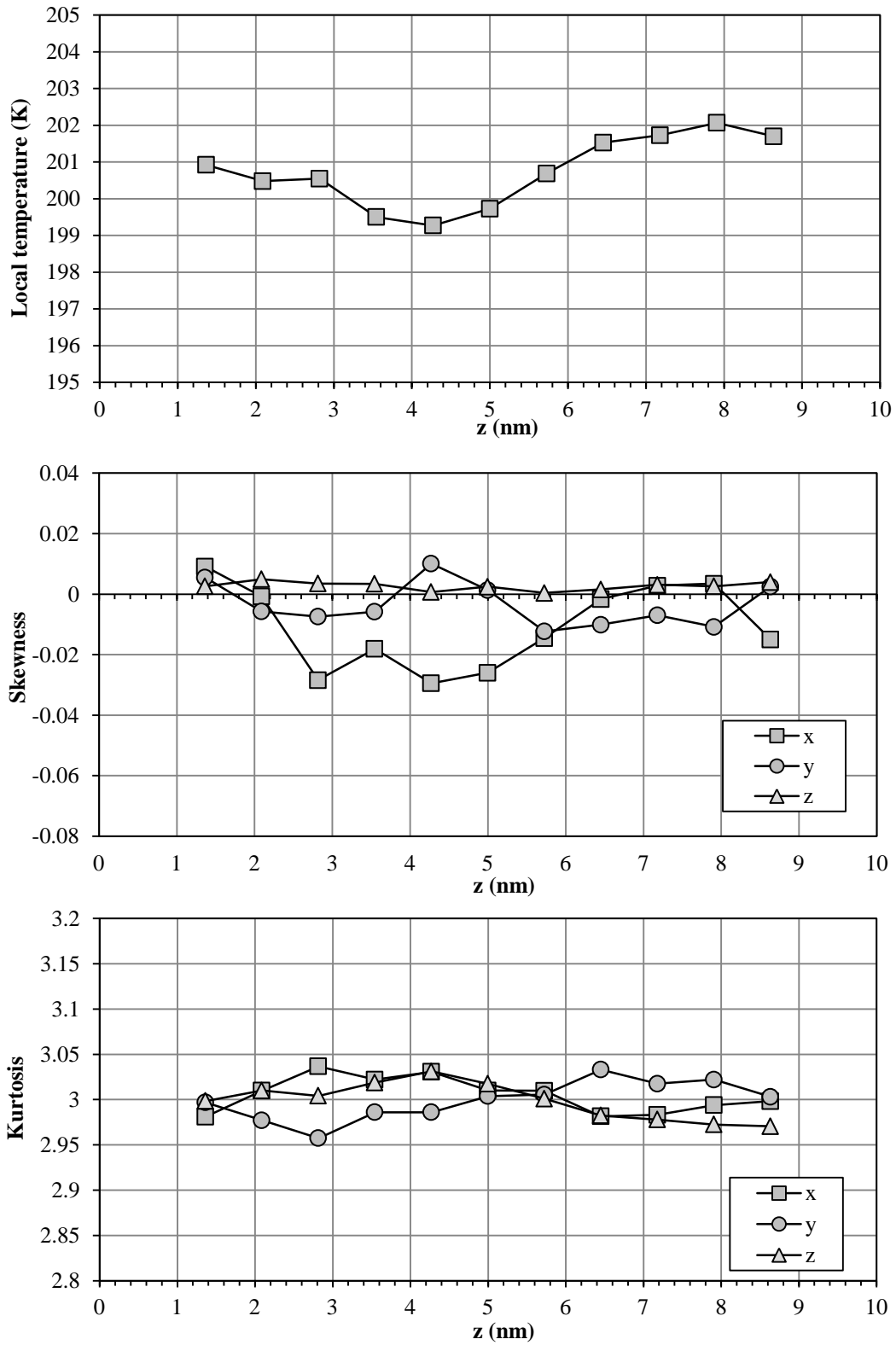


Figure 3.6: Temperature, velocity skewness and velocity kurtosis (gas in equilibrium).

Chapter 4

Heat Diffusion in a Solid-Gas System

In this chapter, we extend the equilibrium MD system to explore the non-equilibrium nature of the gas. First, a steady heat flow was introduced to the system by maintaining a temperature difference between the walls that confine the gas. We find how the temperature, skewness and kurtosis vary across the gap and compare it with equilibrium data that was previously obtained. These data will indicate how far the system deviates from equilibrium behavior. Second, the operating conditions (temperature, pressure, surface resistance and gap size) were varied to explore their effects on heat flux and the effective thermal conductivity of the gas. Third, the system pressure was compared with those predicted by well-known equations of state. Finally, work in this chapter was checked for consistency by inspecting the effect of varying sizes of the unit cell.

4.1 Spatial Variation of Statistical Quantities

Based on the system given in Section 3.2, one wall was set to a temperature of 250 K, while the other wall was set at 150 K. All other operating parameters remain unchanged. The temperature, skewness and kurtosis trends along the L_z were analysed. A temperature gradient was produced as heat diffused through the gas in a steady-state fashion. Temperature slip was also clearly observed.

4.1.1 Skewness

Positive skewness in velocity in the direction of heat transfer can be observed at every slab along z . To visualise skewness, the velocity distribution at the middle slab (centre of unit cell, 5 nm mark) was plotted in Figure 4.1. With reference to Figure 4.2, the skewness in z is approximately 0.28, while velocities in x and y do not skew. The distributions in all three axes have excess kurtosis, which indicate they are not strictly Gaussian. Due to skewness, the probability distribution has a heavier tail on the right and the mode is offset to slightly to the left. Physically, this means that the gas atoms moving from the hot wall to the cold wall generally have more energy compared to the ones moving in the opposite direction. This difference in energy results in the net heat flow.

4.1.2 Kurtosis

Some interesting trends in the kurtosis of velocity can be observed. When compared to the base case, it is apparent that the kurtosis in z deviates from its nominal value of three and increases along z . Kurtosis in x and y also deviate positively, although their trends are not as clear. As opposed to the no heat flow case, the heat flow causes the gas to maintain thermal non-equilibrium which prevents the velocity distributions from attaining Gaussian distributions.

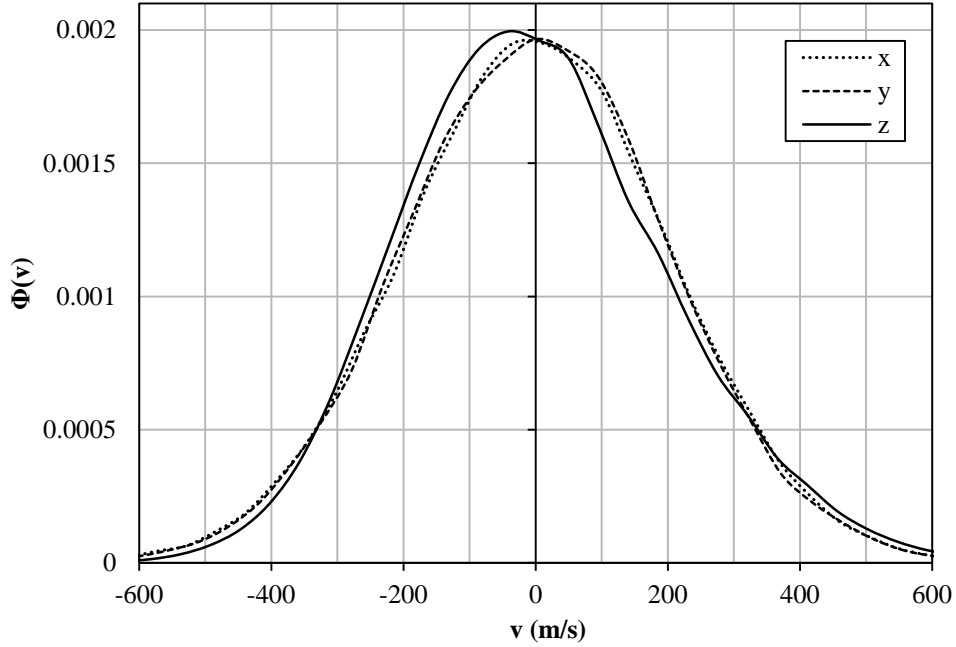


Figure 4.1: The probability distribution of velocity sampled from the middle slab reveals a skewed distribution in z .

One might ask at this point: what is the cause of excess kurtosis in all x , y and z axes? Because the velocity distribution in z must skew for the heat conduction to occur, it is uncertain at this point whether skewness can affect kurtosis. In addition, the density and temperature gradient across z makes it even harder to establish the cause for the increased kurtosis in z . No attempt was made in this work to determine the cause of excess kurtosis in z . However, the increased kurtosis in x and y , whose directions are orthogonal to the heat flow, is as intriguing and we focus our interest here. We postulate that the heat flow, by some mean, can cause kurtosis in z to increase, which in turn lead to the increase in kurtosis in x and y . This coupling of kurtosis between the spatial coordinates will be further investigated in Chapter 5.

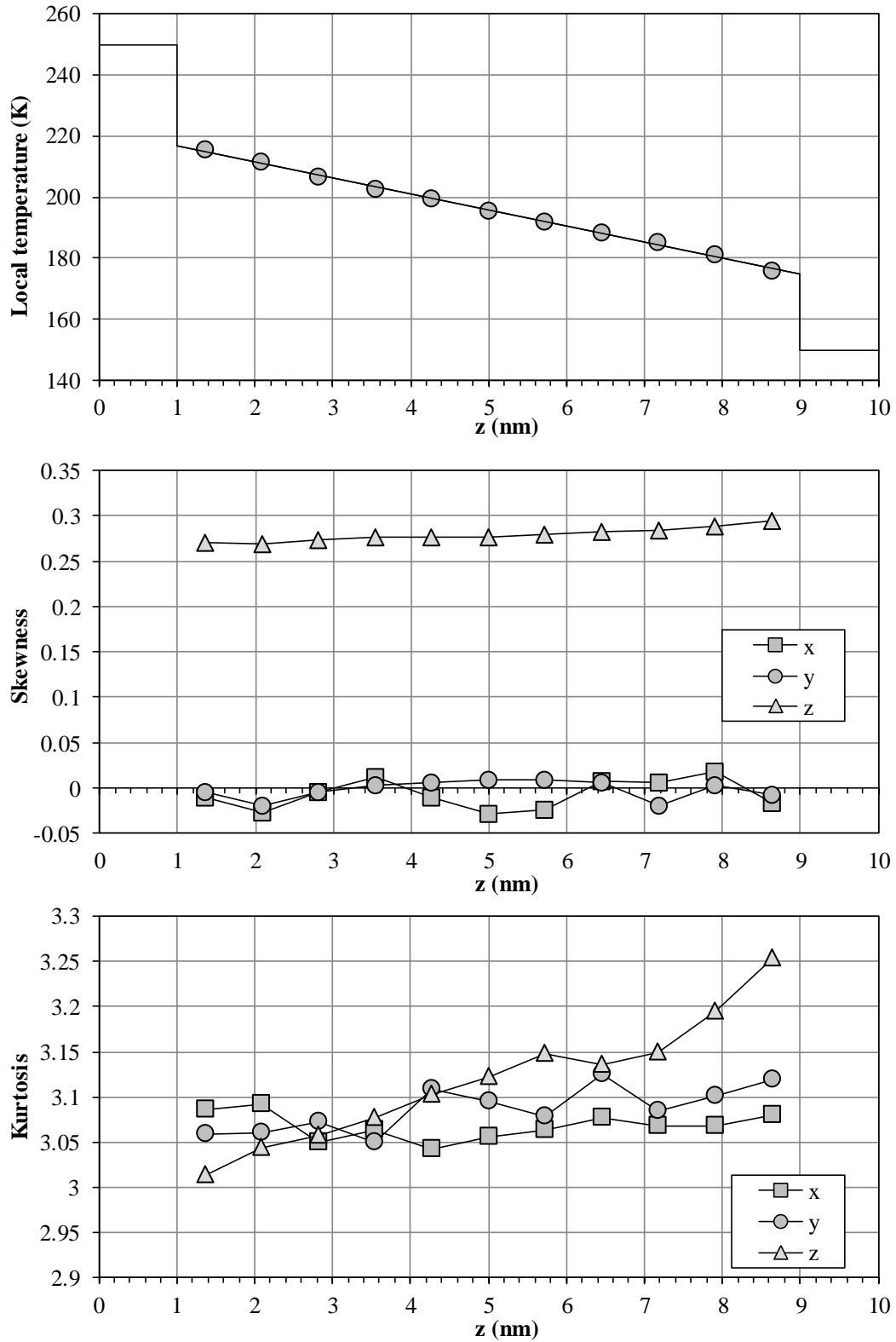


Figure 4.2: Temperature, velocity skewness and velocity kurtosis of the gas under steady-state heat flow. It is informative to compare this with the equilibrium case presented in Figure 3.6 (page 29).

4.2 Spatial Variation of Conditioned Statistical Quantities

In this section, mass, velocity and potential energy data was sampled every instance atoms *cross* imaginary planes that are normal to heat flow, and positioned at the middle (z -direction-wise) of the slabs. This is a way to visualise in greater detail, how mass flux, momentum flux, heat flux and potential energy vary over L_z . To extract more information, data was split into two sets, conditioned upon the direction of travel (sign of v_z) at the point of sampling. For example, as opposed to reporting the *net* mass flux across the plane, the mass flux “going left” ($v_z < 0$) of the plane and the mass flux “going right” ($v_z \geq 0$) of the plane can be distinguished. Their difference will then be the net flux. The number of atoms used was 320 and all other parameters were unchanged.

The conditioned mass flux of the system is shown in Figure 4.3. Although the net mass flux across the system must be conserved, the conditioned mass fluxes are not constant across L_z . This is due to the density gradient produced by the heat flow. It should be noted that the dips in flux near the walls are not physical, but rather an artefact due to the absence of atoms beyond the walls. Implementing a more realistic wall model is likely to address this issue.

From Figure 4.4, it can be observed that the conditioned momentum flux increases slightly with increasing density, but the net flux is a constant. The heat flux (kinetic energy only, Figure 4.5) behaves similarly to the momentum flux. The net heat fluxes across the system are conserved and correspond to the fluxes measured from the walls. However, the conditioned heat fluxes decreases with increasing density.

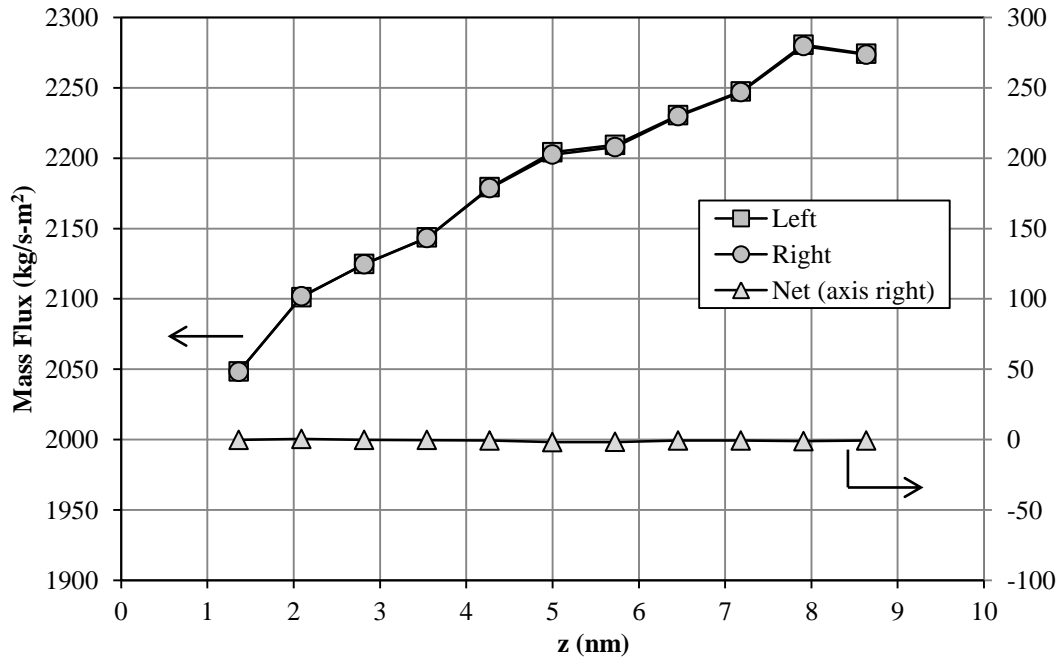


Figure 4.3: Conditioned mass flux, across a hot-to-cold gap. “Left” and “right” refers to the direction of travel of the sampled atoms.

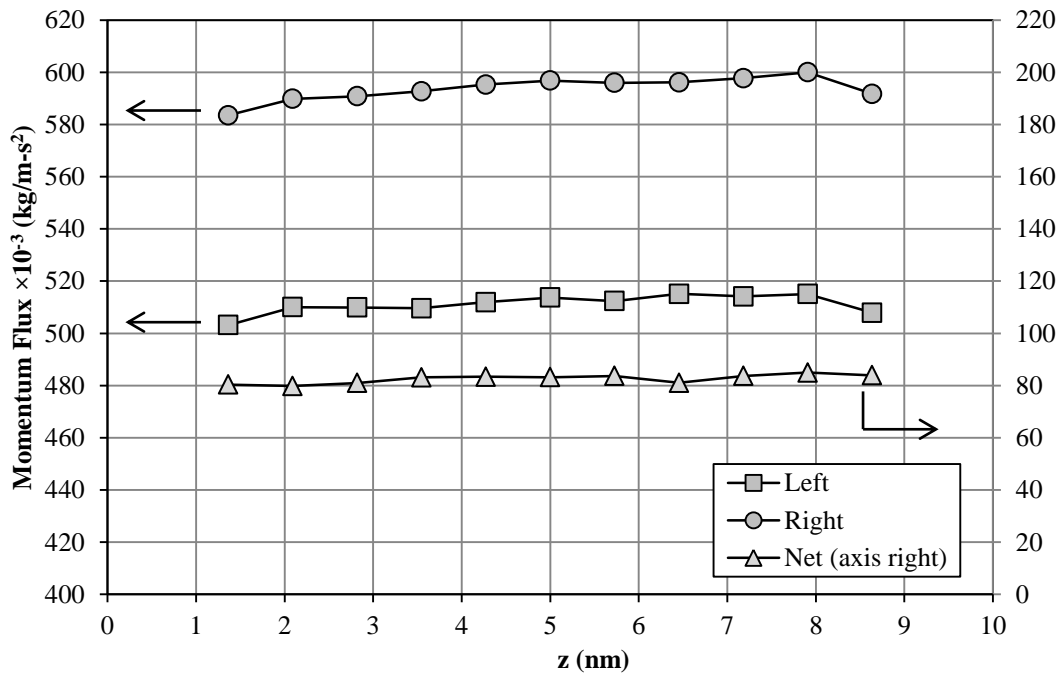


Figure 4.4: Conditioned momentum flux.

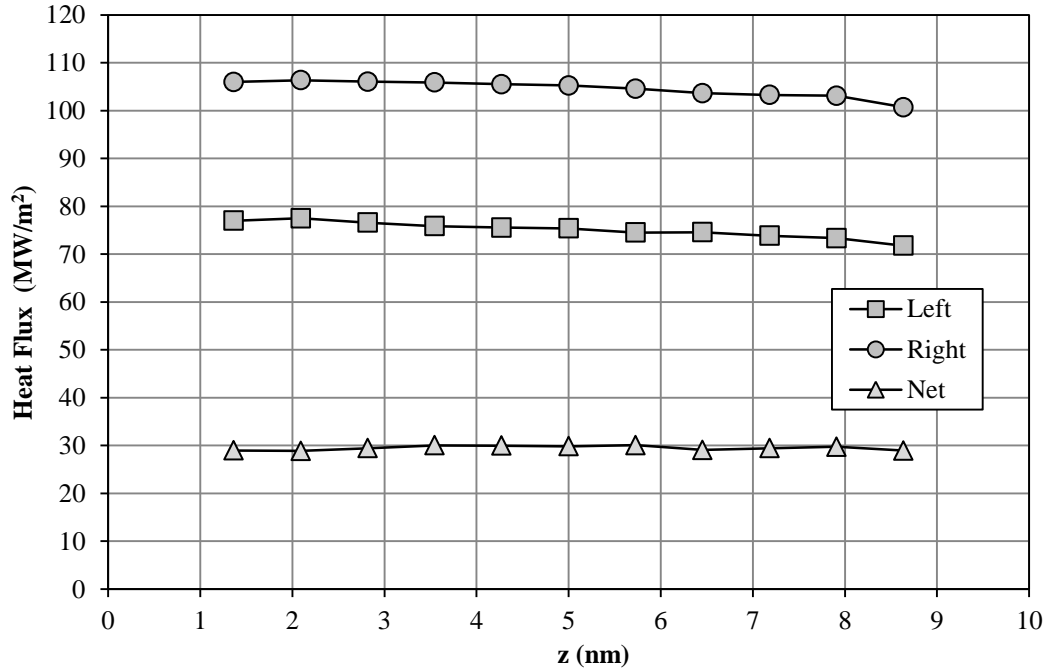


Figure 4.5: Conditioned heat flux.

The downward trend of potential energy (see Figure 4.6) is due to the increased density, since the atoms are positioned closer to each other and experience stronger potentials. The persistent difference between the potential energy of atoms going left versus right is due to the asymmetric distribution of momentum along the direction of heat transfer. As an atom originating from the hot wall (“going right”) has, on average, more kinetic energy than one originating from the cold wall, it will collide with greater impact and gain larger potentials during the repulsion that follows a collision.

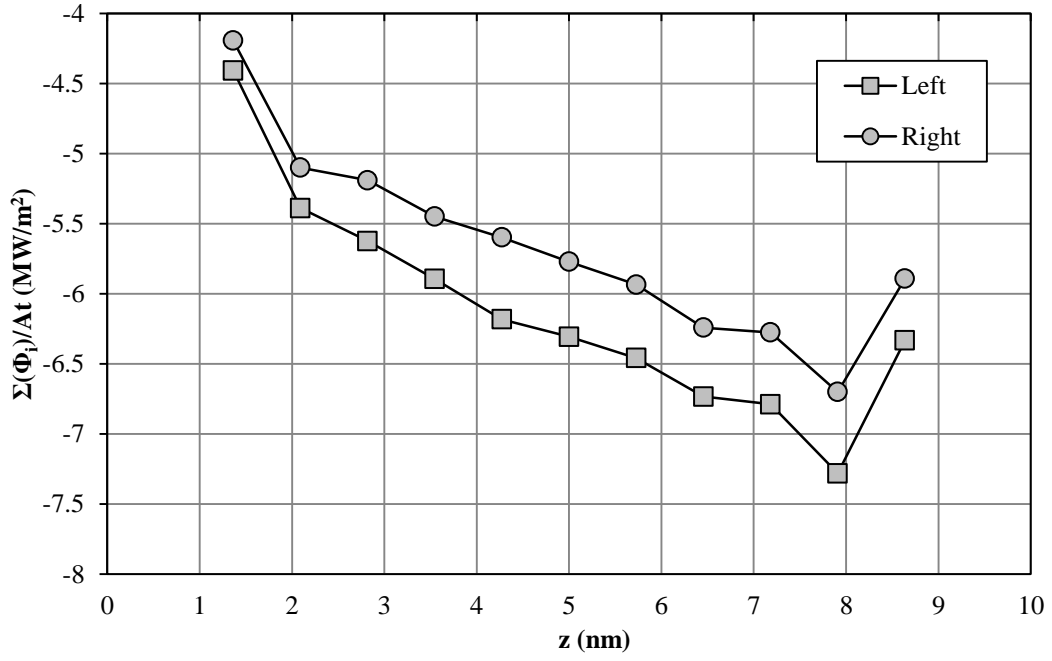


Figure 4.6: Conditioned total potential energy, normalised by area and time.

4.3 Heat Flux

4.3.1 Effect of Pressure

To vary the system's pressure, the number of gas atoms used and the dimensions of the unit cell were adjusted. Gap sizes were fixed at 6, 8 and 10 nm. For each setup, the lateral dimensions of the unit cell were made somewhat larger than the longest mean free path of the gas to minimise the effect from the periodic boundaries. Again, the wall temperatures were fixed at 250 K and 150 K. The heat flux through the system was computed using Eq. (2.20) and plotted in Figure 4.7.

It was observed that the magnitude of heat flux increases with pressure. This is caused by the increased rate of impingement by the heat carriers (gas atoms) on the wall. We note that gap size has little effect on heat flux at low pressures but at elevated pressures, small gap sizes will result in a larger flux.

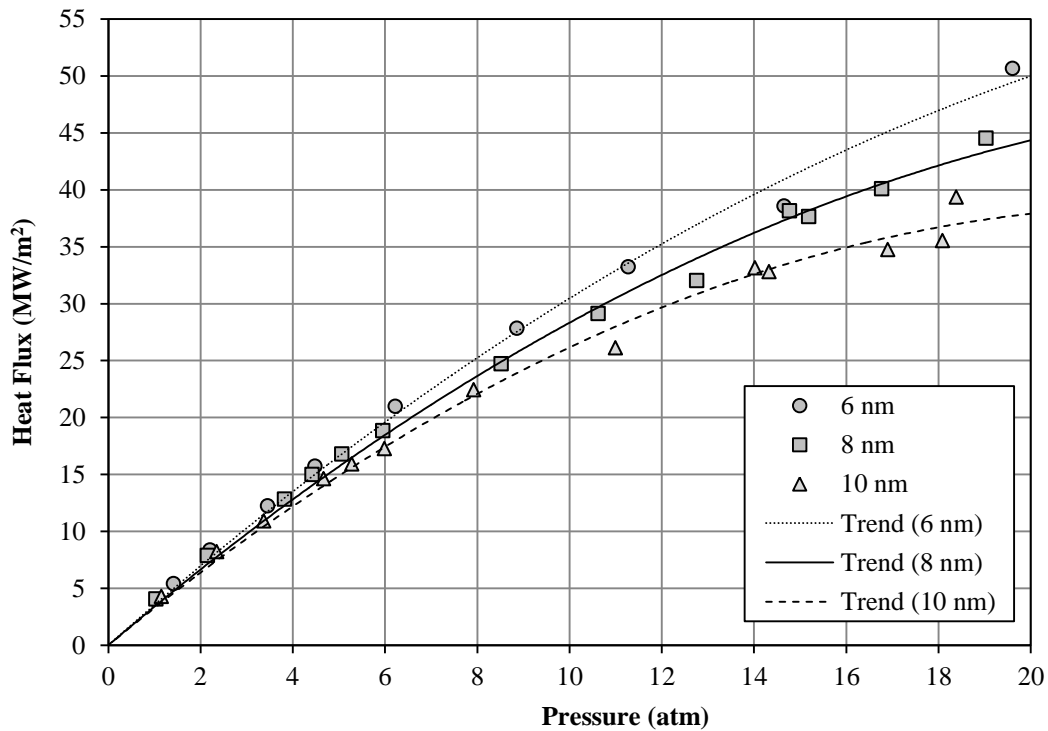


Figure 4.7: Heat flux versus system pressure at various gap sizes. Trend lines serve only to guide the eye.

4.3.2 Effect of EAC

The effect of EAC (α) on heat flux was studied here. Both walls were set to the same α and the gap size and pressure was fixed at 6 nm and 11.3 atm, respectively. The results are plotted in Figure 4.8.

One application of the results obtained here is the determination of the theoretical maximum flux. For example, under the same operating conditions, one can expect a flux no greater than the one determined when $\alpha = 1$. Another possible application is to estimate α of the wall material if the flux is known. Since α for most real metals are in the order of 0.01 to 0.1 [15], a curve with higher precision about that region may be necessary to be of practical use.

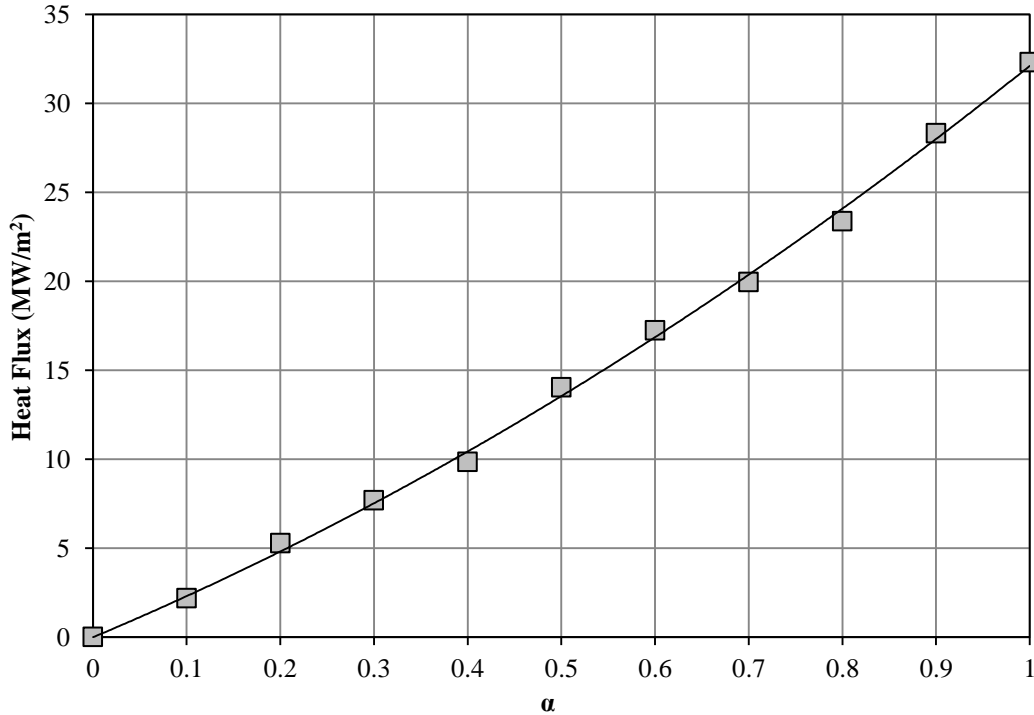


Figure 4.8: Heat flux versus EAC.

α can also affect the temperature gradient. From Figure 4.9, it can be observed that the temperature gradient increases with heat flux. It can be confirmed that the interfacial temperature slip is non-diminishing with respect to α . Tabulated results from this section can be found in Table 4.1 located at the end of this chapter.

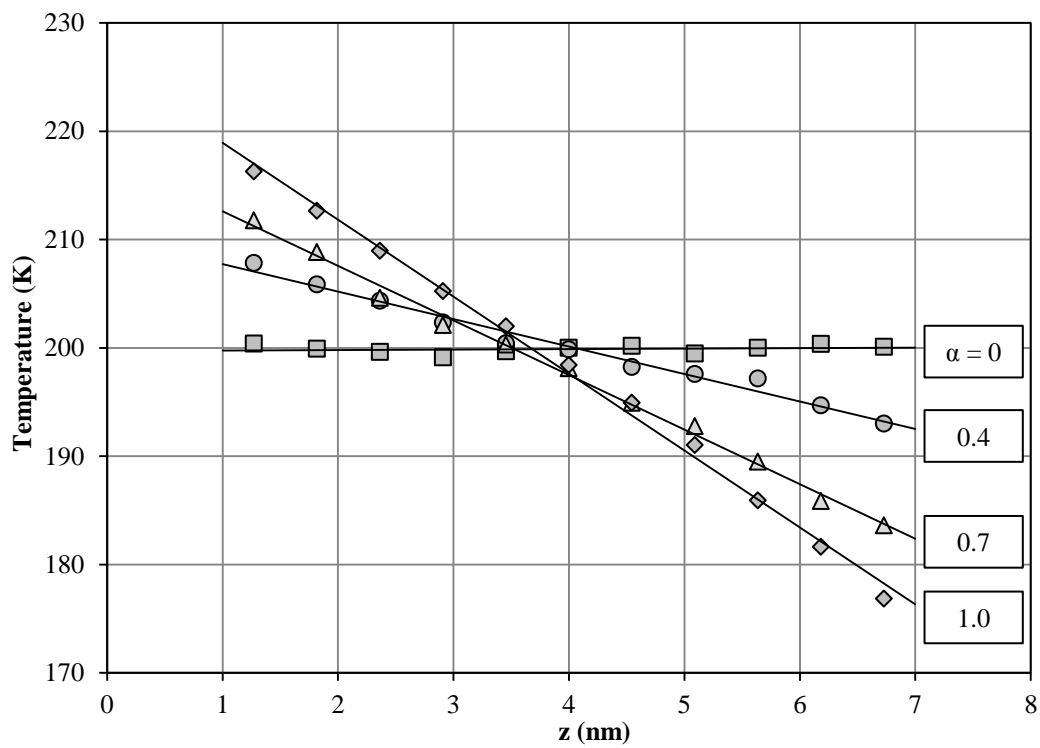


Figure 4.9: Select temperature gradients versus EAC (labelled), for comparison.

4.4 Thermal Conductivity

4.4.1 Fourier's Law

The Fourier's law of heat conduction is given by

$$\dot{\mathbf{q}} = -\kappa A \nabla T \quad (4.1)$$

where $\dot{\mathbf{q}}$ is the rate of heat flow and κ is the thermal conductivity. For one-dimension heat conduction, Eq. (4.1) can be reduced and rearranged to

$$\kappa = -\frac{\dot{q}_z}{A} / \frac{dT}{dz} \quad (4.2)$$

Since $\frac{dT}{dz}$ can be estimated by performing a linear regression of the temperatures sampled from the slabs, and the heat flow (q_z) through the reflective boundaries can be computed from Eq. (2.20), we can make use of the results to estimate the *effective* thermal conductivity of argon across the gap. Linear regression also yields the standard error [18] of the estimated gradient, which was used to find the magnitude of error propagated to κ .

4.4.2 Thermal Conductivity of an Ideal Gas

For *diffusive* one-dimension heat conduction by an ideal gas, the thermal conductivity can be found by [19]:

$$\kappa = \frac{1}{3} \frac{C_{V,m} \lambda N}{N_A V} v_{ave} \quad (4.3)$$

where v_{ave} is the average speed of the gas particles and is given by $v_{ave} = \sqrt{8k_B T / \pi m}$. $C_{V,m} = \frac{3}{2} k_B$ for an ideal, monatomic gas. The mean free path, λ , can be found from Eq. (2.9). With some algebraic manipulation, it can be shown that

$$\kappa = \frac{k_B}{D_\sigma} \sqrt{\frac{k_B T}{\pi m}} \quad (4.4)$$

The theoretical thermal conductivity of an ideal gas is only a function of \sqrt{T} and is independent of pressure. We assume diffusive heat conduction only if $\lambda/L_z > 1$. This means that Eq. (4.4) is only valid when the system is above certain pressures (when the mean free path is short enough). This theoretical thermal conductivity will be used as a reference for comparison with the results from Fourier's Law.

4.4.3 Effect of Pressure and Temperature

The pressure and temperature were varied and their effects on effective thermal conductivity was studied. From Figure 4.10, it can be seen that the effective thermal conductivity of argon increases with pressure as it deviates from ideal gas behaviour. This is because at high pressures, the interatomic forces are significant and the ideal gas assumption required for Eq. (4.4) becomes invalid. However, as of analytical expectations (where $\kappa \propto \sqrt{T}$), higher temperatures result in higher thermal conductivity.

At low pressures, the mean free path of the gas exceeds the size of the gap and *ballistic* heat conduction dominates over diffusive heat conduction. In ballistic heat conduction, high energy atoms emanating from the hot wall travel directly to the cold wall, without collision with other atoms along the way. In this regime, the thermal conductivity is a stronger function of pressure compared to the diffusive heat transfer regime (i.e. $\frac{d\kappa}{dP}_{ballistic} > \frac{d\kappa}{dP}_{diffusive}$). The diminishing temperature dependence of thermal conductivity was also observed at low pressures.

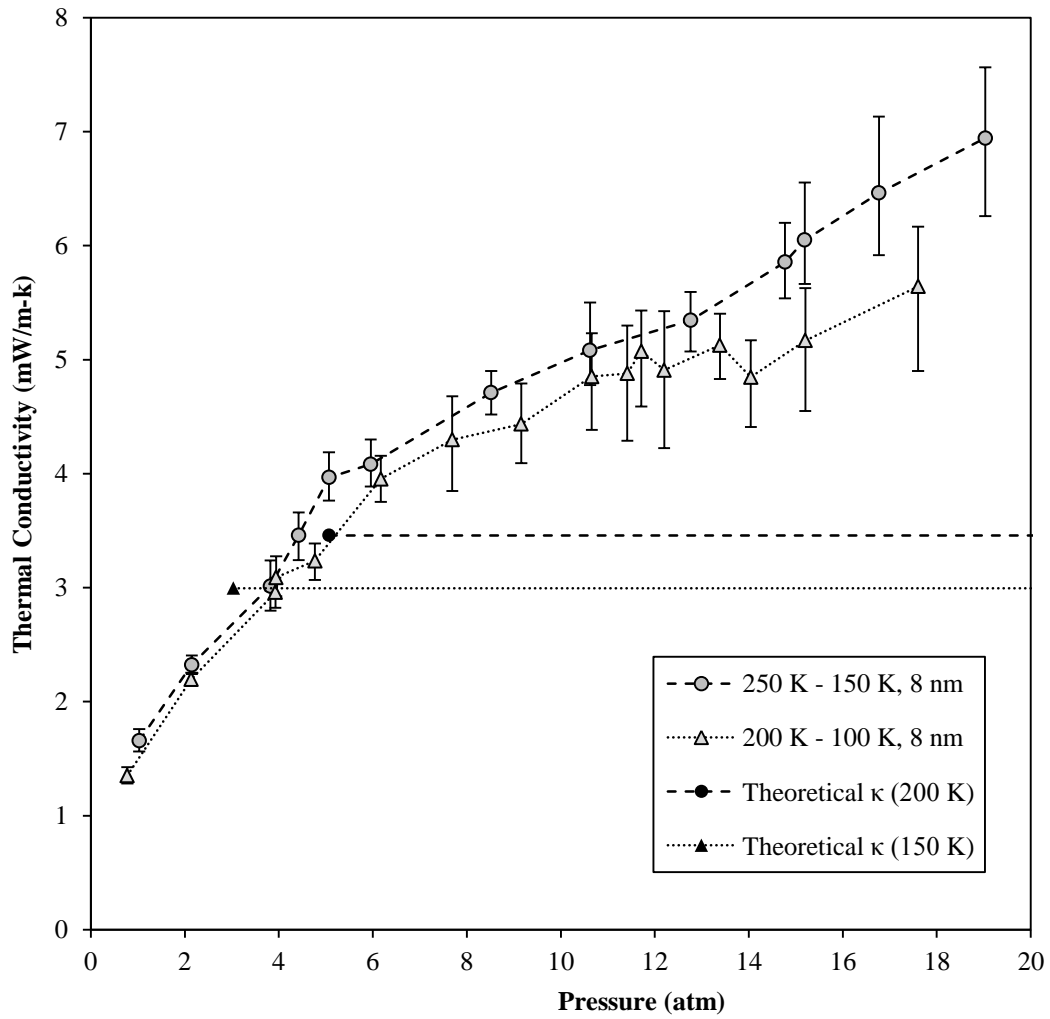


Figure 4.10: κ versus system pressure at two temperatures (95% confidence intervals shown).

4.4.4 Effect of Pressure and Gap Size

The pressure and gap size was varied its effect on effective thermal conductivity was studied. From Figure 4.11, it can be seen that reducing the gap size causes the effective thermal conductivity to decrease. Similar to temperature dependence, the dependence on gap size also diminishes at low pressures. Tabulated results on the effective thermal conductivity of argon under various temperatures, pressures and gap sizes (from this section and Section 4.4.3) can be found at the end of this chapter, in Tables 4.2 through 4.5.

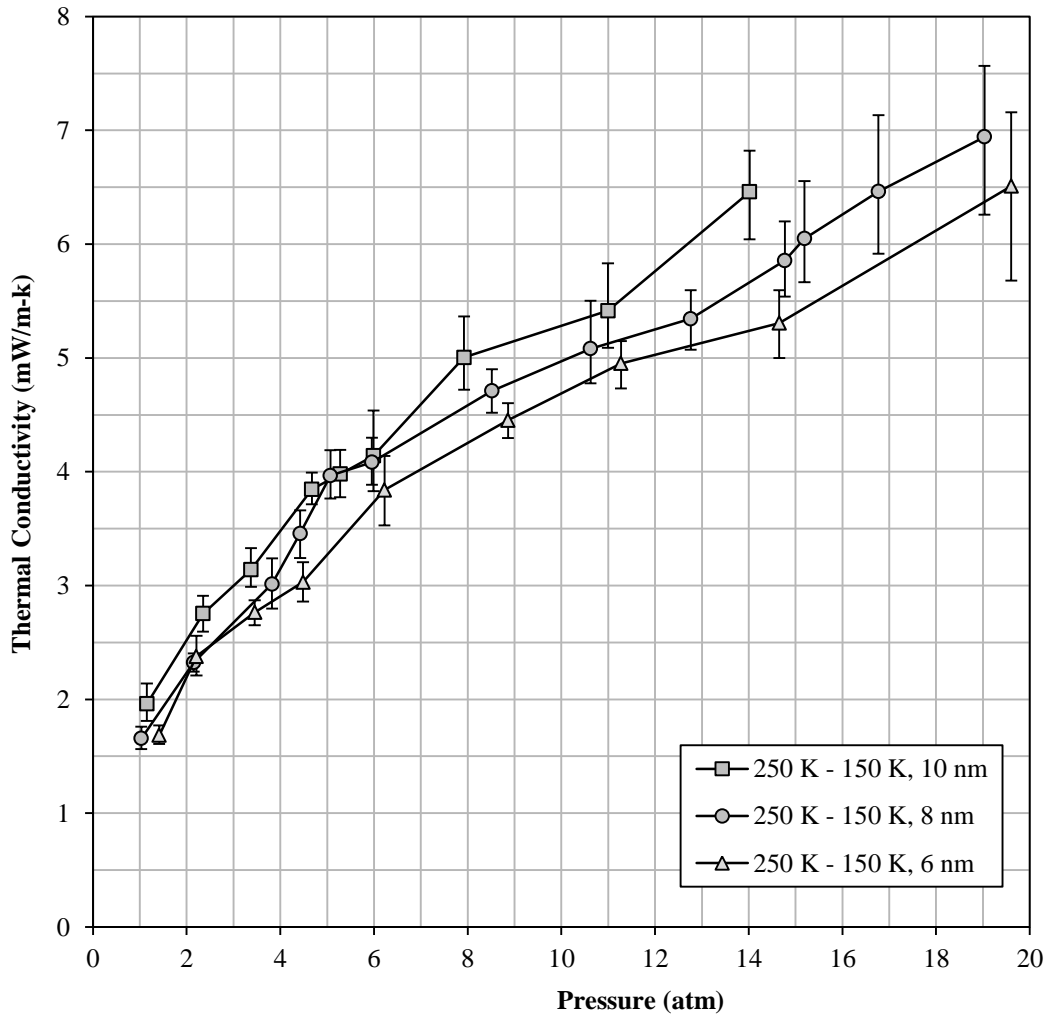


Figure 4.11: κ versus system pressure at various gap sizes (95% confidence intervals shown).

4.5 System Pressure

The ideal gas behaviour of argon is studied here by comparing the pressure obtained from the simulation with predictions by three well-known equations of state (EOS) – ideal gas, van der Waals, and Redlich-Kwong (R-K). Since argon atoms do not have acentricity, three-parameter equations of state such as the Soave-Redlich-Kwong and Peng-Robinson equations were not considered. The pressure of the system was computed by Eq. (2.19).

As a review, the ideal gas equation of state is given by

$$P = \frac{nRT}{V} \quad (4.5)$$

and the van der Waals equation of state is given by

$$P = \frac{nRT}{V - nb} - \frac{n^2a}{V^2} \quad (4.6)$$

where

$$a = \frac{27R^2T_c^2}{64P_c} \quad \text{and} \quad b = \frac{RT_c}{8P_c}.$$

and lastly, the R-K equation of state is given by

$$P = \frac{nRT}{V - nb} - \frac{n^2a}{\sqrt{T}V(V + nb)} \quad (4.7)$$

where

$$a = \frac{R^2T_c^{5/2}}{9P_c(2^{1/3} - 1)} \quad \text{and} \quad b = \frac{(2^{1/3} - 1)RT_c}{3P_c}.$$

The critical pressure of argon used is 48.0 atm (4.86 MPa) and the critical temperature is 150.7 K [20]. The prediction error in pressure was calculated by

$$\text{Pressure Deviation} = \frac{P - P_{EOS}}{P} \times 100\% \quad (4.8)$$

where P is the system pressure computed by Eq. (2.19) while P_{EOS} is from Eqs. (4.5), (4.6) or (4.7). Pressure deviations are plotted respectively in Figures 4.12, 4.13 and 4.14.

As expected, the ideal gas equation was found inadequate when the pressure is large and the temperature is low. At such extreme conditions, the error in pressure is almost 15%. On the other hand, the van der Waals and R-K equations of state can predict the pressure accurately over a wide range of pressures – where errors are within $\pm 2\%$.

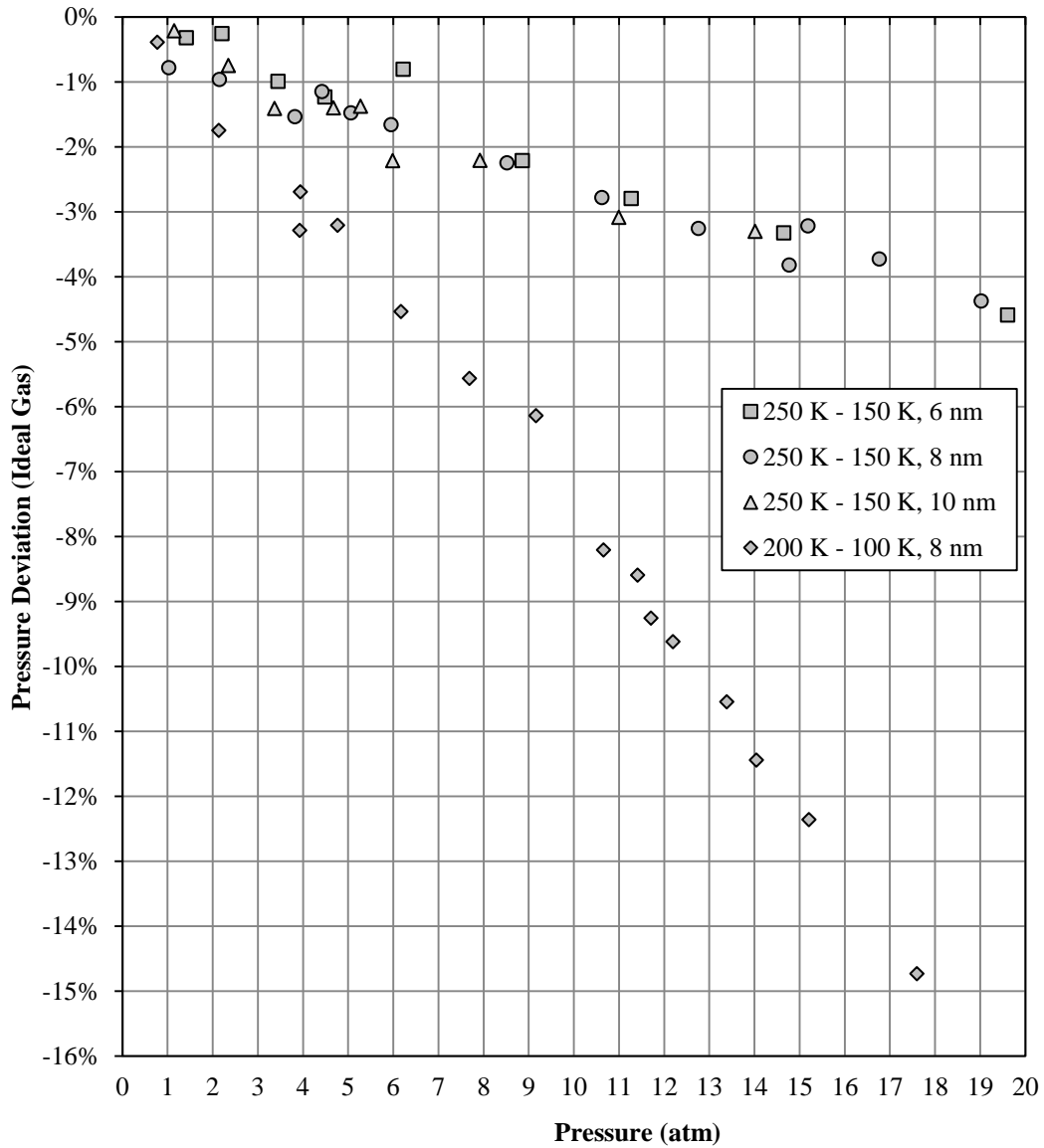


Figure 4.12: Deviation from pressure predicted by the ideal gas equation.

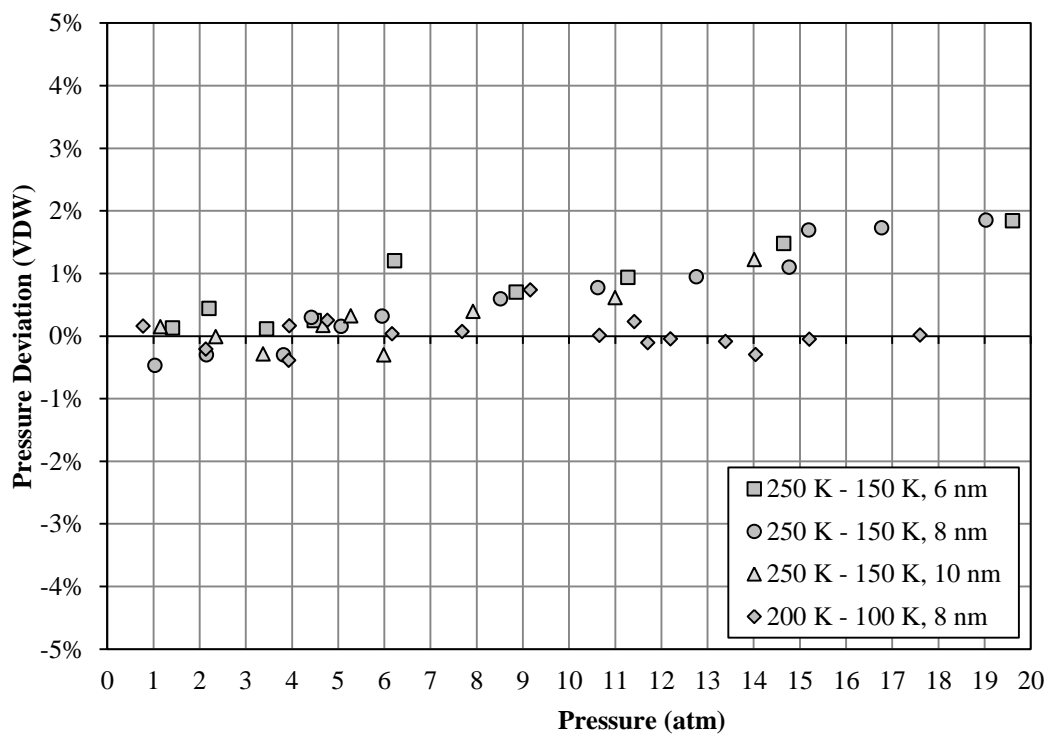


Figure 4.13: Deviation from pressure predicted by the van der Waals equation.

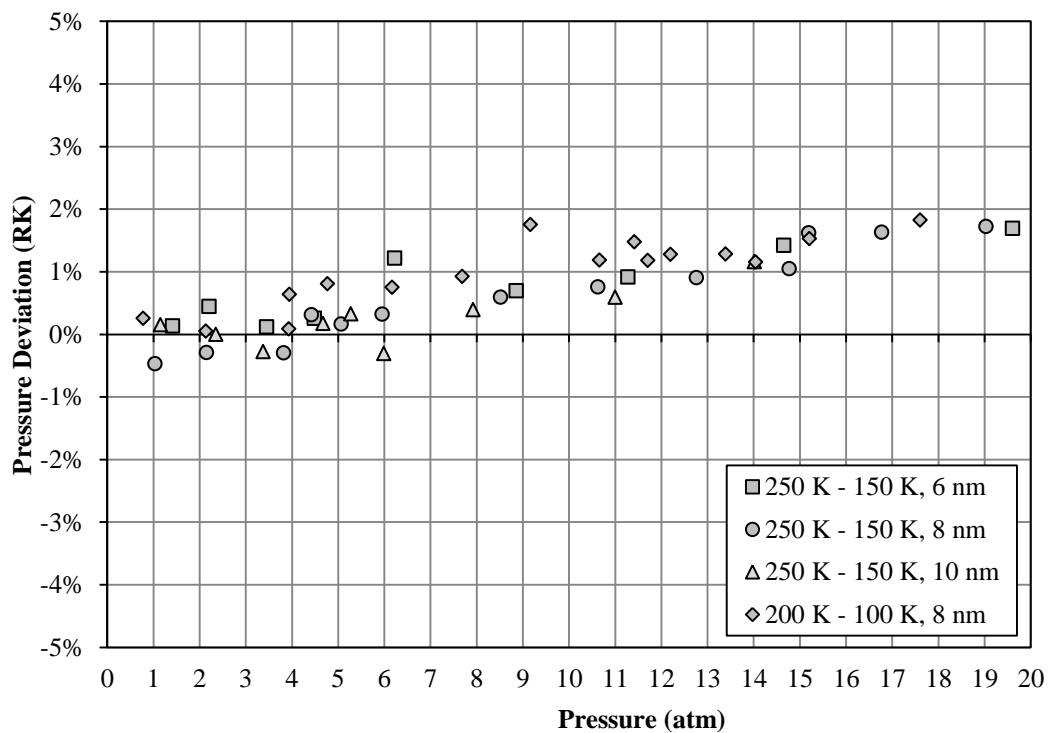


Figure 4.14: Deviation from pressure predicted by the R-K equation.

4.6 Verification

4.6.1 System Size

In practice, the size of the unit cell is kept large enough for good statistics yet not redundantly large for a tractable computation time. Here, the size of the unit cell was varied in the lateral directions while the pressure was kept constant by adjusting the number of atoms. This is to verify that the system size is indeed large enough. Without dispute, the thermal conductivity and all other time-averaged, intensive properties must be independent of size of the unit cell.

The gap size was fixed at 6 nm, with $T_W = 250$ K and 150 K, and $P = 11.3$ atm. It was found that the thermal conductivity was essentially independent of system size when more than 200 atoms were used (see Figure 4.15).

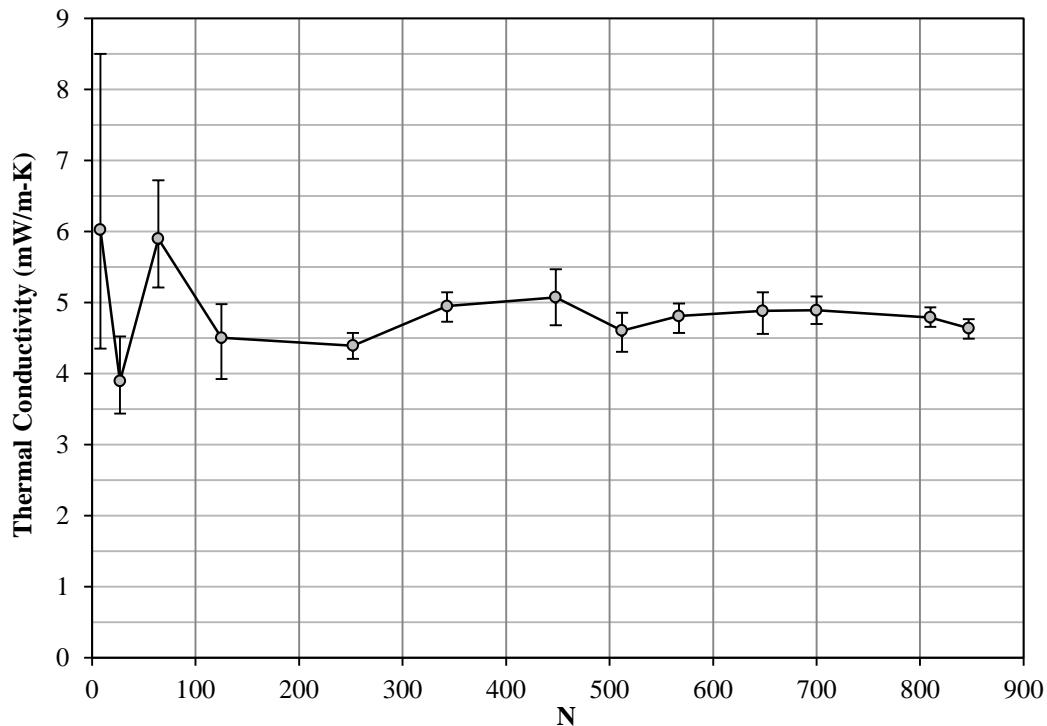


Figure 4.15: Measured κ versus system size (95% confidence intervals shown).

4.6.2 Computer Time

Using the same set of data from Section 4.6.1, the computation time versus the number of atoms was plotted in Figure 4.16. Due to the implementation of neighbour lists and cut-off potentials, computer time scales linearly with the number of atoms.

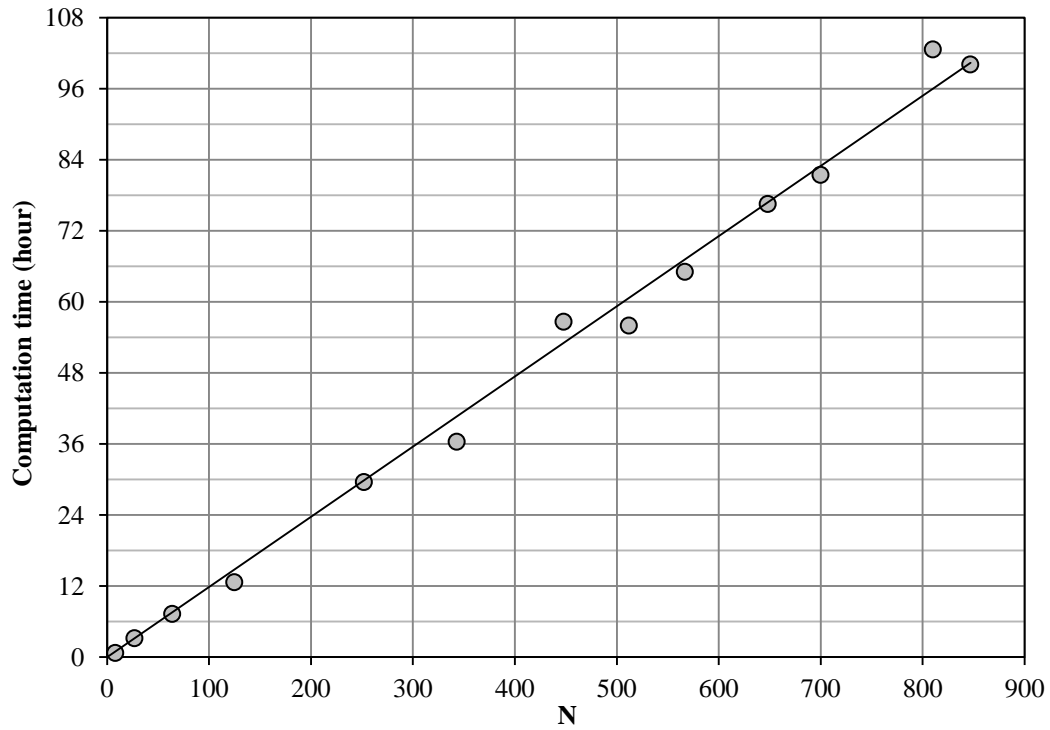


Figure 4.16: Computer time versus system size.

Table 4.1: Tabulated results for $T_W = 250$ K and 150 K, $L_z = 6$ nm, $P = 11.3$ atm over various α . *Note: κ computed with small heat fluxes are numerically inaccurate as $Q/\frac{dT}{dz}$ is indeterminate as $Q \rightarrow 0$.

α	Q MW/m ²	$\Delta T/\Delta z$ K/nm	κ mW/m-K
0.0	0	0	-
0.1	2.51	-0.49	5.13*
0.2	5.05	-1.88	2.69*
0.3	7.97	-1.98	4.03
0.4	10.2	-2.53	4.02
0.5	14.1	-3.56	3.96
0.6	17.5	-4.11	4.26
0.7	20.2	-5.03	4.01
0.8	24.1	-5.65	4.27
0.9	28.4	-6.16	4.61
1.0	33.1	-7.09	4.66

Table 4.2: Tabulated results for $T_W = 250$ K and 150 K, $L_z = 6$ nm.

N	L_x, L_y nm	P atm	Q MW/m ²	κ mW/ m-K	λ/L_z	λ/L_x
800	50.0	1.41	5.43	1.68	4.8	0.58
800	40.0	2.21	8.35	2.38	3.1	0.46
800	32.0	3.45	12.2	2.76	2.0	0.37
800	28.0	4.48	15.6	3.03	1.5	0.32
512	19.0	6.22	20.7	3.84	1.1	0.34
343	13.0	8.86	28.1	4.45	0.76	0.35
343	11.5	11.3	33.2	4.95	0.60	0.31
216	8.00	14.7	38.8	5.31	0.46	0.34
216	6.90	19.6	50.0	6.51	0.34	0.30

Table 4.3: Tabulated results for $T_W = 250$ K and 150 K, $L_z = 8$ nm.

N	$L_x L_y$ nm	P atm	Q MW/m ²	κ mW/ m-K	λ/L_z	λ/L_x
800	50.7	1.03	4.06	1.66	5.0	0.78
512	28.0	2.15	7.88	2.32	2.4	0.68
512	21.0	3.82	12.8	3.01	1.3	0.51
512	19.5	4.42	14.8	3.46	1.1	0.47
512	18.2	5.07	16.8	3.97	1.0	0.44
512	16.8	5.96	18.8	4.08	0.85	0.41
512	14.0	8.52	24.7	4.71	0.59	0.34
320	9.90	10.6	29.3	5.08	0.47	0.38
384	9.90	12.8	32.2	5.34	0.39	0.32
448	9.90	14.8	37.8	5.86	0.34	0.27
252	7.37	15.2	38.4	6.05	0.33	0.36
252	7.00	16.8	40.5	6.46	0.30	0.34
288	7.00	19.0	44.8	6.94	0.26	0.30

Table 4.4: Tabulated results for $T_W = 250$ K and 150 K, $L_z = 10$ nm

N	L_x, L_y nm	P atm	Q MW/m ²	κ mW/ m-K	λ/L_z	λ/L_x
800	43.0	1.15	4.26	1.96	3.6	0.83
800	30.0	2.35	8.27	2.75	1.7	0.58
800	25.0	3.37	11.0	3.14	1.2	0.48
512	17.0	4.67	14.6	3.85	0.87	0.51
800	20.0	5.28	15.9	3.98	0.77	0.39
512	15.0	5.99	17.6	4.14	0.68	0.45
512	13.0	7.92	22.4	5.00	0.51	0.39
512	11.0	11.0	26.3	5.41	0.37	0.33
343	8.00	14.0	33.2	6.46	0.29	0.36

Table 4.5: Tabulated results for $T_W = 200$ K and 100 K, $L_z = 8$ nm.

N	L_x, L_y nm	P atm	Q MW/m ²	κ mW/ m-K	λ/L_z	λ/L_x
800	50.0	0.78	3.43	1.35	4.8	0.77
800	30.0	2.14	8.49	2.20	1.7	0.46
800	22.0	3.93	14.2	2.96	0.93	0.34
800	22.0	3.94	14.4	3.09	0.93	0.34
800	20.0	4.77	16.5	3.24	0.77	0.31
512	14.0	6.17	20.8	3.95	0.59	0.34
320	9.90	7.69	23.3	4.30	0.47	0.38
384	9.90	9.16	26.3	4.43	0.39	0.32
343	8.60	10.7	29.7	4.85	0.33	0.31
343	8.30	11.4	31.0	4.88	0.31	0.30
252	7.00	11.7	29.9	5.07	0.30	0.34
343	8.00	12.2	31.2	4.91	0.29	0.29
288	7.00	13.4	33.9	5.13	0.26	0.30
252	6.36	14.0	33.9	4.85	0.25	0.31
252	6.09	15.2	35.4	5.17	0.23	0.30
252	5.60	17.6	38.8	5.64	0.19	0.27

Chapter 5

Velocity Kurtosis of a Gas System – Dynamics and Anisotropy

In this chapter, we attempt to explain the excess kurtosis found in the velocity distribution that is perpendicular to the steady-state heat flow. All walls were removed from unit cell and replaced with periodic boundaries. The system was artificially pushed out of equilibrium by introducing excess kurtosis in one arbitrary direction. This was accomplished by a kurtosis controller that can manipulate velocity using a differential scaling technique. The kurtosis in the other two directions were analysed for change.

5.1 Motivation

The effect of higher moments of velocity statistics in one direction on the other directions is not a new knowledge. To illustrate this, consider an isolated monatomic gas system in thermal equilibrium. Due to energy equipartition, one can expect the variance (σ^2 , the second moment) of velocity in all directions to be equal. Suppose, there exist a mechanism that now perturbs the equilibrium by forcing and fixing the variance of one arbitrary direction (say, x -axis) to a new value. The gas system will respond by redistributing its energies to attain a new equilibrium state, where the variances of the other two directions (y - and z -axis) have changed to match the new variance. This response by the gas system can be modelled as a dynamic process, where the input can be seen as σ_x^2 and the outputs are variances orthogonal (\perp) to the input: namely, σ_y^2 and σ_z^2 . The steady-state gains for both outputs are exactly one, meaning, for every one unit of change in the input, there is an equal corresponding change in the outputs.

On another hand, the third standardised moment, skewness (S), or in fact any odd-numbered moments, do not influence other directions. Since skewness is an indication of heat conduction in the gas, skewness cannot propagate this way – for that will imply an unphysical 90° direction change of heat flow. Not surprisingly, the propagation of skewness between directions was at no time observed in this work (see Figure 4.2). Again, if this response of skewness to skewness is considered a dynamic process, we can safely assume the steady-state gain is zero.

We move on to the fourth standardised moment, kurtosis (γ). Will the presence of velocity kurtosis in some direction ($\gamma_{v\parallel}$) induce kurtosis in other orthogonal directions ($\gamma_{v\perp}$), just like variance? Or will it behave like skewness, where the $S_{v\perp}$ is essentially unaffected by $S_{v\parallel}$? The extent or even possibility of this phenomenon is not as obvious. Again, if we consider the response of kurtosis as a dynamic process, the magnitude of its steady-state gain will answer these questions. If the steady-state gain can be found to be statistically non-zero, this will allow the conclusion that in a steady-state heat flow system, $\gamma_{v\parallel}$ can somehow propagate to $\gamma_{v\perp}$. Furthermore, if the steady-state gain is unity, it will indicate isotropy of kurtosis – somewhat resembling energy equipartition.

5.2 Kurtosis Controller Characterisation

The constant-energy feedback kurtosis controller (henceforth “*kurtostat*”¹) was newly introduced in Section 2.6.2. Before an attempt to apply it in an MD simulation, we test the *kurtostat* here so that its character can be better understood. To do so, a *static* set of data containing 10^7 normally distributed random numbers with zero mean and unity variance was generated. Then, the *kurtostat* was set at $\tau = 50$ and $\gamma_0 = 6$ and was used to transform the dataset over 100 iterations.

Figure 5.1 shows the evolution of the dataset’s probability distribution. It can be seen that the dataset, which was initially Gaussian, transitions into a smooth distribution that has a heavier tail and sharper peak. Figure 5.2 shows the change in kurtosis over iterations. As expected, the kurtosis of the dataset was increased smoothly by the *kurtostat* from 3 to 6. The rate of change of kurtosis is dependent on γ the time constant of the *kurtostat*. At $\text{iter.} = \tau$, γ/γ_0 is almost 96 %, which indicates that it is faster than a first-order process (63.2 % expected).

Clearly a drawback of the *kurtostat*, the skewness of the dataset was also altered, although by a much smaller extent. This is due to the symmetric redistribution of velocities by the *kurtostat* that will cause any initial skewness to be amplified. The impact on skewness arising out of *kurtostat* action in an actual MD simulation can be found in a later section (Section 5.4.4).

¹For the convenience of addressing – *kurtostat* is a word combination of *kurtosis* and *stat*, where suffix *-stat* is “the combining form used in devices for stabilising (*thermostat*, etc.) [21]”.

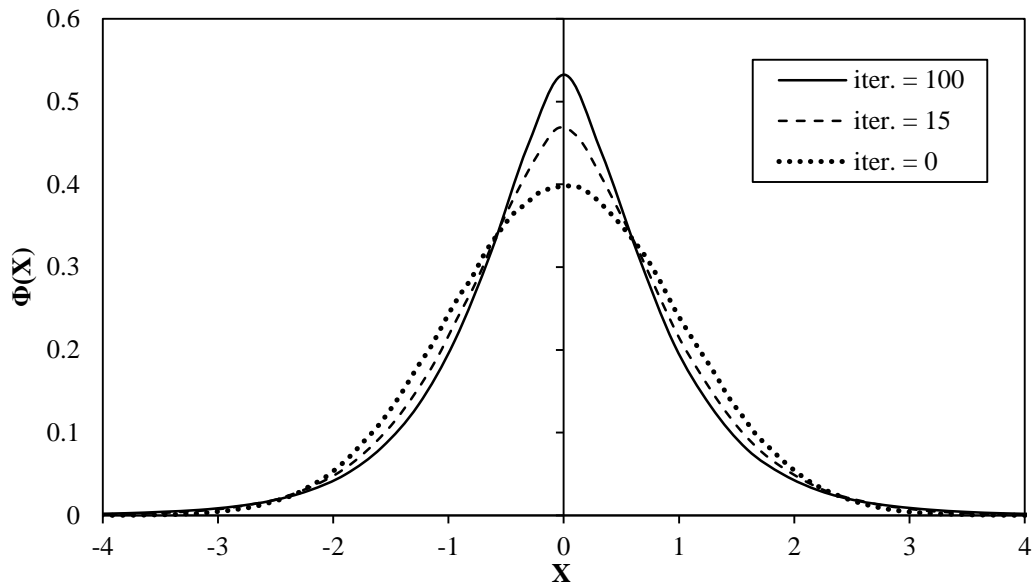


Figure 5.1: Evolution of the probability distribution of the dataset.

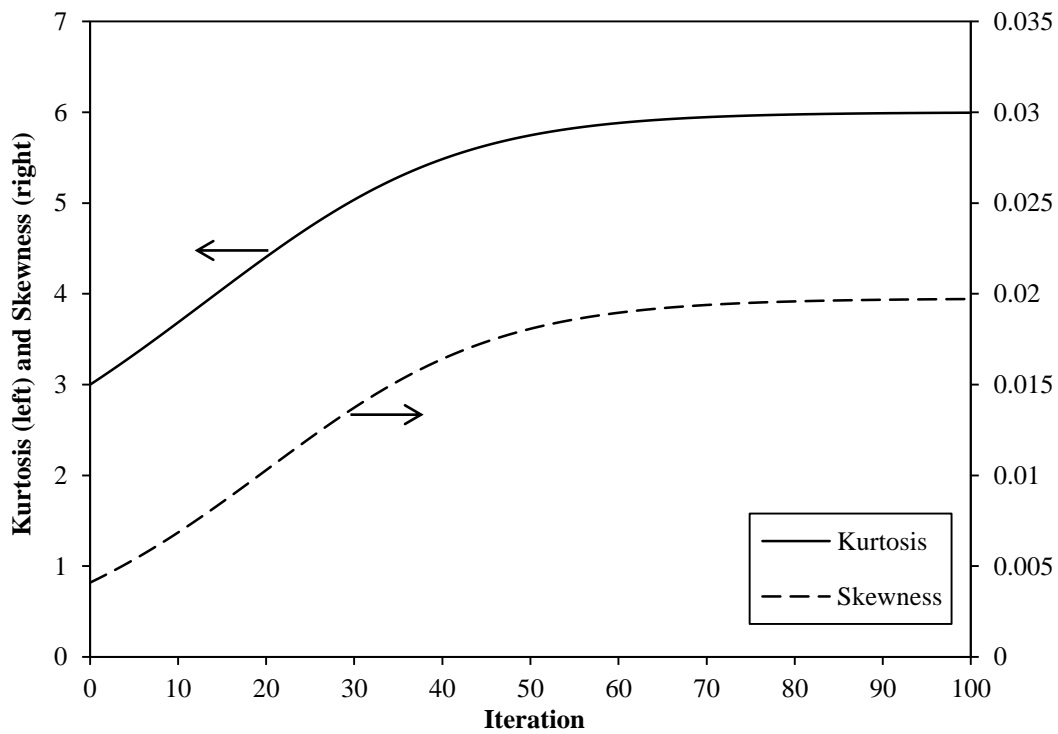


Figure 5.2: Kurtosis and skewness of the dataset over iterations.

5.3 Simulation Setup

The unit cell measures $14 \times 14 \times 10$ nm and contains 512 argon atoms, exerting a pressure of 6.9 atm. Periodic boundaries were placed in *all* directions. The temperature of the system was brought to 200 K using the thermostat and was switched off after 100 ps. Similar to simulation setups in previous chapters, the thermostat only serves to bring the system to the desired initial temperature. In the absence of kurtostat action, this setup is a microcanonical ensemble.

The input to the system (defined u) is the kurtosis in one arbitrary axis and the output (defined y_1 and y_2) is the kurtosis in the other two axes. In reality, kurtosis in the x -axis was made the input but this choice is only a matter of convention and is inconsequential to the results. The kurtostat was set at $\tau = 10^4$ and target kurtosis $\gamma_0 = 6$, and was activated only between 2 and 7 ns to perturb the system. The simulation horizon was 10 ns.

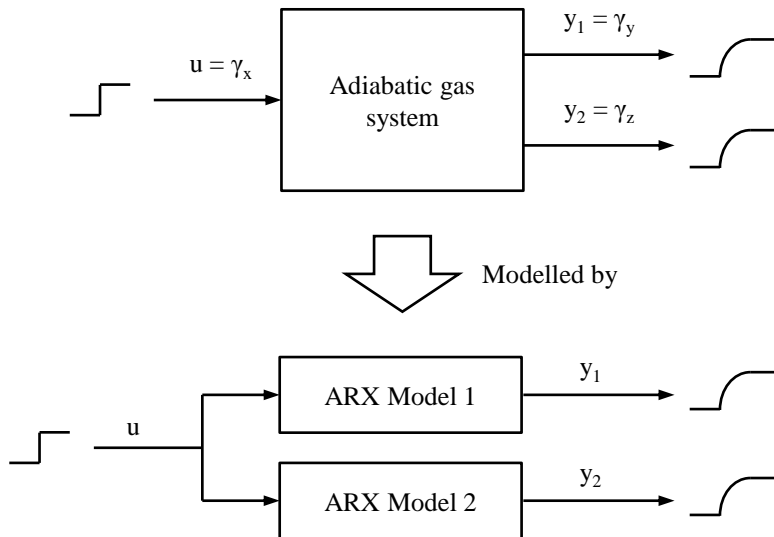


Figure 5.3: Block diagram of the system showing the relationship between the ARX models, input and output.

5.4 Results and Discussion

5.4.1 Input Signal and Output Response

Figure 5.4 shows the resulting input signal and output responses. Kurtostat action produced an input signal that approximates a square pulse of 3 excess kurtosis in amplitude and 5 ns in width. It was noted that the system rapidly regains equilibrium when the kurtostat was switched off at 7 ns. The output response was considerably noisier but some gain is still discernible from the plots.

5.4.2 Steady-State Gain and Error

The input and output data was collected and fitted with two first-order ARX models to determine the process steady-state gains, first-order time constants and time delays. It should be noted that the input signal does not provide sufficient excitation, and hence the time constant and the time delay can only serve as rough estimates. The steady-state gains were found to be:

$$K_{ss,1} = 0.15807 \pm 0.02639$$

and

$$K_{ss,2} = 0.15767 \pm 0.02081$$

To visualise the dynamics, the unit step response with error intervals of the models are plotted in Figure 5.5. It became clearer that the steady-state gains were indeed well above zero but much less than unity. It should be noted that the exact numerical value of this steady-state gain is immaterial here since the objective was limited to proving that a non-trivial gain exists for kurtosis. The value of the steady-state gain is likely to be a complicated function of the physical properties of the gas used. In addition, the extent of nonlinearity of the process is unknown, so only qualitative arguments can be made with confidence here. Complicated nonlinear dynamics is expected and it deserves a detailed study separate from this work.

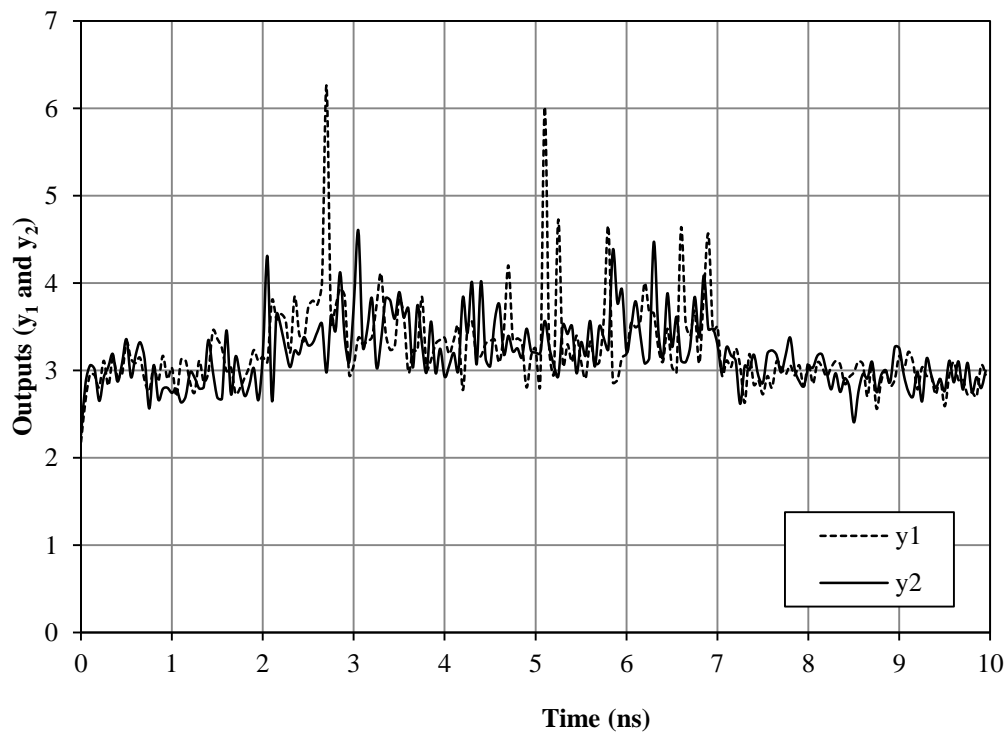
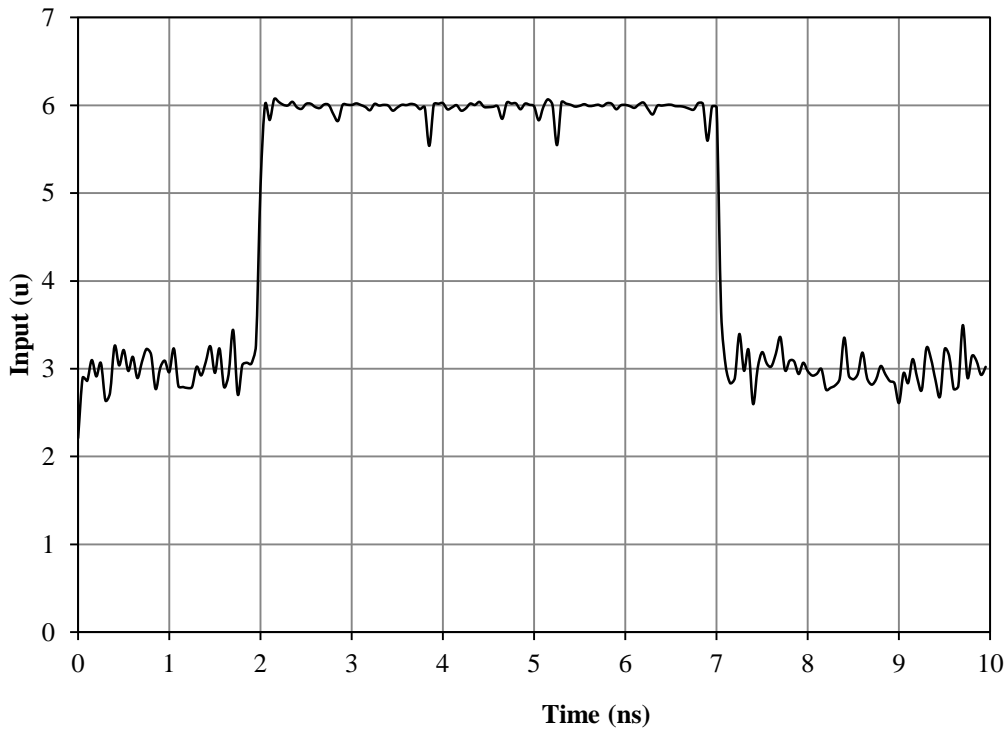


Figure 5.4: Input signal and output response of the system. Data points are downsampled for clarity.

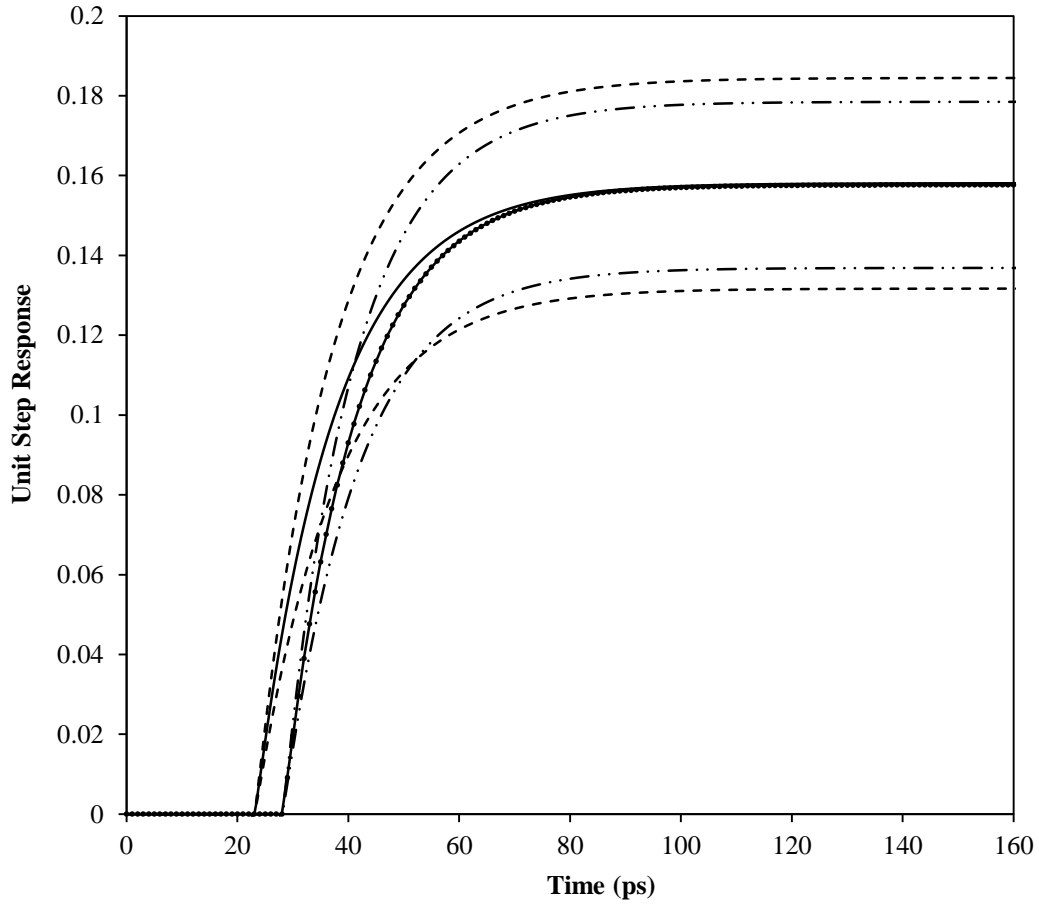


Figure 5.5: The solid line (—) and the dotted solid line (—•) are the unit step responses of the ARX models for y_1 and y_2 . Broken lines (---) and (-·-) are their 95 % confidence intervals, respectively.

5.4.3 System Noise and Choice of Target Kurtosis

As the system produces very noisy output data, a high signal-to-noise ratio input is required. To illustrate this, the resulting fit on data for one output is plotted in Figure 5.6. It can be seen that if the input was any weaker, the change in output will become so small that any gain will start to overlap the background noise and numerical methods used to estimate the steady-state gain will return excessively large error intervals. This is why a high target kurtosis (γ_0) of 6, which may arguably be unrealistic, had to be chosen.

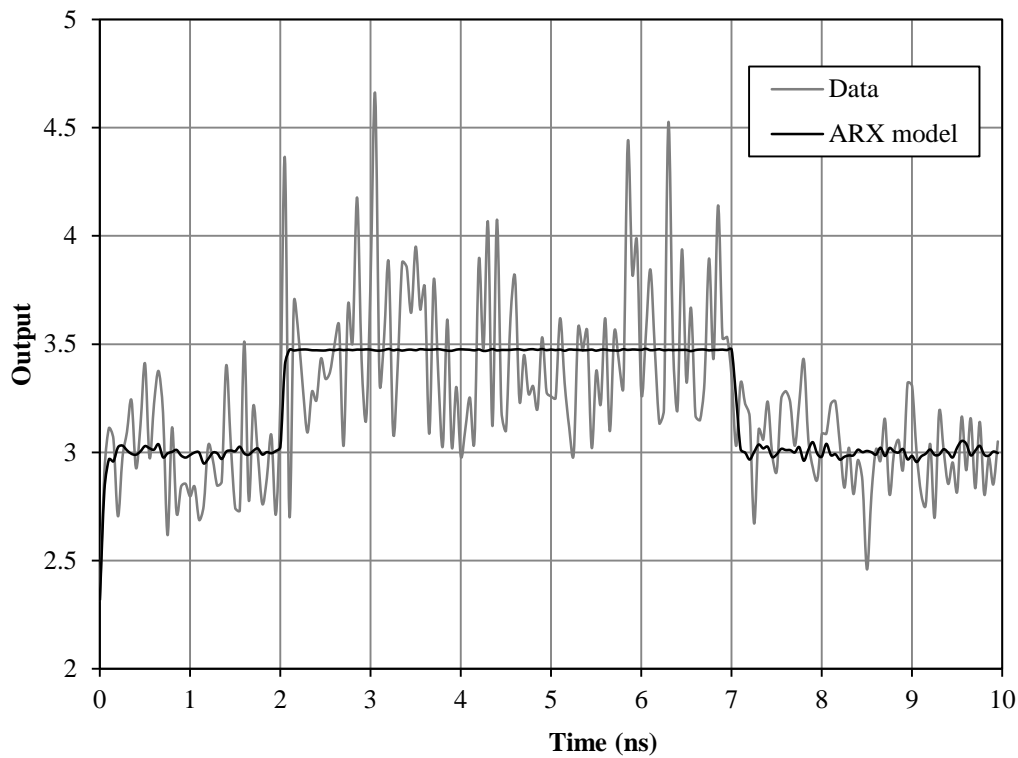


Figure 5.6: Fit on noisy data by the ARX model. The fit for the other output is very similar and is not shown.

5.4.4 Impact on Skewness by Kurtostat

From Figure 5.7, it can be observed that the skewness of the input axis fluctuate more when under control by the kurtostat. However, due to the self-equilibrating nature of molecular chaos, any generated skewness tend to dissipate. This is in contrast with the observation from the previous test setup in Section 5.2, where the error in skewness accumulates over time.

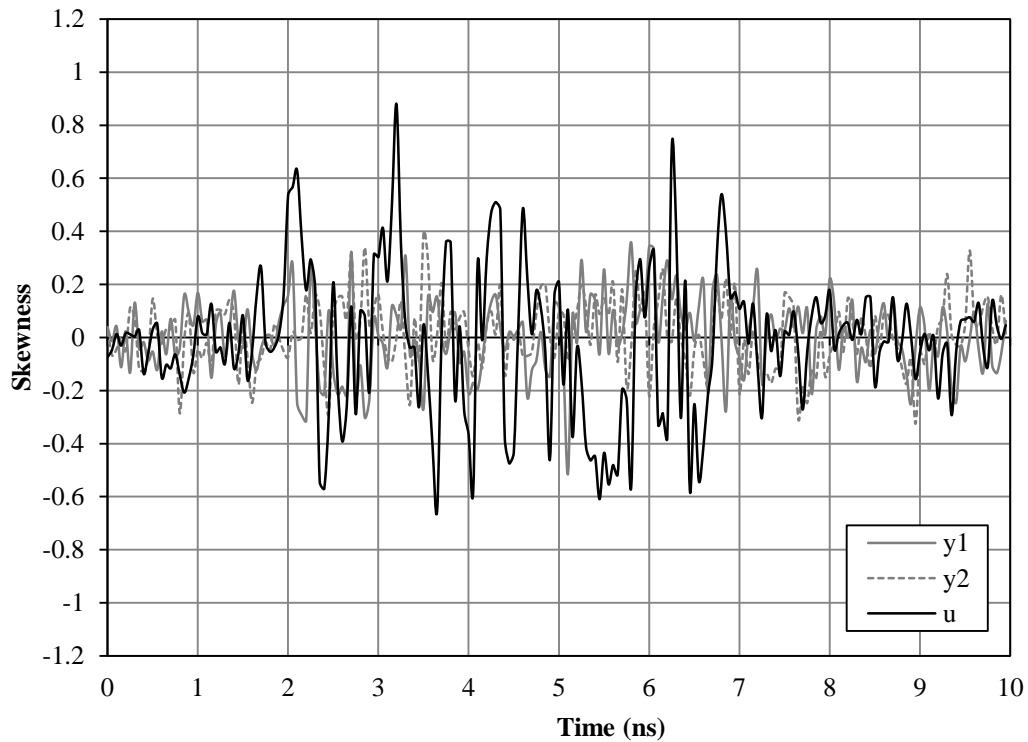


Figure 5.7: Skewness in all three axes over time. The increase in fluctuation is apparent between 2 and 7 ns, which is the period the kurtostat is active.

Chapter 6

Conclusions

Equilibrium systems containing argon gas that was sandwiched between two walls were simulated. Regardless of wall interactions, both constant-energy and constant-temperature ensemble data showed that the velocity distributions of the gas were independent of position, density and wall geometry. The velocity distributions of the gas sampled across the gap was found to be Gaussian by computing their skewness and kurtosis.

Steady-state heat flow was introduced to the gas by maintaining a temperature difference between the walls that confine it, creating a non-equilibrium system. As a result, skewness in velocity was produced in the direction of thermal conduction. The kurtosis of velocity distribution in the direction of heat flow was found to increase with increasing gas density. In addition, kurtosis orthogonal to the heat flow was also found to deviate from nominal values. The intricate coupling of the heat flux, skewness, density gradient, temperature gradient to kurtosis was not fully explored in this work and deserves further investigation.

Conditioned statistics provide more insight to the mechanisms of heat transfer. It was shown that the difference in momentum and kinetic energy resulted in heat transfer. Potential energy difference was found to occur due to the imbalance of momentum of atoms moving from hot to cold and those moving in the opposite direction. Further work can be done to implement a more realistic wall model and address the boundary artefacts.

In all operating conditions considered in this work, the effective thermal conductivity of the gas generally increased with increasing pressure, temperature and gap size. However, the dependence on temperature and gap size diminished at low pressures ($P < 5$ atm, $\lambda/L_z > 1$). The system pressure was found to be within $\pm 2\%$ of that predicted by the van der Waals and R-K equations of state.

A newly developed constant-energy feedback kurtosis controller, which was referred to as a kurtostat, was successfully applied to control the kurtosis of static and dynamic distributions. The kurtostat was used to push a gas system away from equilibrium without introducing any form of heat flow and the resulting temperature and density gradients. It was found that a non-trivial gain of approximately 0.16 exists for kurtosis of velocity distributions orthogonal to each other. This showed that the velocity kurtoses, although orthogonal, were coupled and were not independent.

Bibliography

- [1] N. Metropolis, A. Rosenbluth, M. Rosenbluth, A. Teller, E. Teller, Equation of state calculations by fast computing machines, *The journal of chemical physics* 21 (1953) 1087.
- [2] G. S. Fishman, *Monte Carlo: concepts, algorithms, and applications*, Springer, 1996.
- [3] F. Ercolessi, *A molecular dynamics primer*, 1997.
URL <http://www.fisica.uniud.it/~ercolessi/md/>
- [4] P. S. Laplace, *A Philosophical Essay on Probabilities*, English translation of the French original by FW Truscott and FL Emory, Dover, New York, 1951.
- [5] B. Alder, T. Wainwright, *Studies in molecular dynamics. i. general method*, *The Journal of Chemical Physics* 31 (1959) 459.
- [6] A. Rahman, *Correlations in the motion of atoms in liquid argon*, *Phys. Rev* 136 (2A) (1964) 405–411.
- [7] L. Verlet, *Computer experiments on classical fluids. i. thermodynamical properties of lennard-jones molecules*, *Physical Review* 159 (1) (1967) 98.
- [8] W. G. Hoover, *Computational Statistical Mechanics*, 1st Edition, Elsevier Science Publishers Ltd., Essex, UK, 1991.
- [9] D. J. Evans, W. G. Hoover, *Flows far from equilibrium via molecular dynamics*, *Annual review of fluid mechanics* 18 (1) (1986) 243–264.
- [10] P. Clause, M. Mareschal, *Heat transfer in a gas between parallel plates: Moment method and molecular dynamics*, *Physical Review A* 38 (8) (1988) 4241.
- [11] R. K. Shukla, V. K. Dhir, *Numerical study of the effective thermal conductivity of nanofluids*, *Proceedings of the ASME Summer Heat Transfer*, July 17 22.

- [12] G. S. Hwang, M. Kaviany, Molecular dynamics simulation of effective thermal conductivity of vapor-filled nanogap and nanocavity, *Journal of Applied Physics* 106 (2) (2009) 024317–024317.
- [13] I. McDonald, K. Singer, Calculation of thermodynamic properties of liquid argon from lennard-jones parameters by a monte carlo method, *Discuss. Faraday Soc.* 43 (0) (1967) 40 – 49.
- [14] D. E. Sanders, A. E. DePristo, Metal/metal homo-epitaxy on fcc (001) surfaces: Is there transient mobility of adsorbed atoms?, *Surface Science* 254 (1-3) (1991) 341 – 353. doi:10.1016/0039-6028(91)90666-G.
URL <http://www.sciencedirect.com/science/article/pii/003960289190666G>
- [15] F. Goodman, Thermal accommodation coefficients, *The Journal of Physical Chemistry* 84 (12) (1980) 1431–1445.
- [16] H. Berendsen, J. Postma, W. Van Gunsteren, A. DiNola, J. Haak, Molecular dynamics with coupling to an external bath, *The Journal of Chemical Physics* 81 (1984) 3684.
- [17] B. Huang, R. Kadali, Dynamic modeling, predictive control and performance monitoring: A data-driven subspace approach, Vol. 374, Springer Verlag, 2008.
- [18] S. S. Rao, *Applied Numerical Methods for Engineers and Scientists*, 1st Edition, Prentice Hall Professional Technical Reference, 2001.
- [19] T. Engel, P. Reid, *Thermodynamics, Statistical Thermodynamics and Kinetics*, Pearson Education, Inc., 2006.
- [20] T. Daubert, R. Danner, Dippr project 801 data compilation, tables of physical and thermodynamic properties of pure compounds (1990).
- [21] Online etymology dictionary.
URL <http://dictionary.reference.com/browse/stat>